BACHELOR'S THESIS

TESTING THE USE OF QUATERNIONS IN THE DESCRIPTION OF THE GRAVITATIONAL WAVE SIGNAL OF PRECESSING BINARY SYSTEMS

Maria de Lluc Planas Llompart

Degree in Physics

Faculty of Sciences

TESTING THE USE OF QUATERNIONS IN THE DESCRIPTION OF THE GRAVITATIONAL WAVE SIGNAL OF PRECESSING BINARY SYSTEMS

Maria de Lluc Planas Llompart

Bachelor's Thesis

Faculty of Sciences

University of the Balearic Islands

Academic Year 2019-20

Key words:

General relativity, black holes, gravitational waves, waveform modelling, spin precession, rotations description, Euler angles, quaternions.

Thesis Supervisor's Name: Sascha Husa

Tutor's Name (if applicable): Sascha Husa

The University is hereby authorized to include this project in its institutional repository for its open consultation and online dissemination, for academic and research purposes only.	Author		Supervisor	
	Yes	No	Yes	No
	☒	☐	☒	☐

1   Introduction

Gravitational-wave astronomy has opened a new window to the universe, providing hitherto hidden information [1], [2]. Even though gravitational waves were already predicted in 1916 [3], their direct detection had major implications in astronomy and fundamental physics. They render possible new tests for General Relativity and carry information about their sources that are complementary to any other "messenger", like photons, neutrinos, or cosmic rays. Furthermore, gravitational waves very weakly interact with matter, making them hard to detect, but also allowing them to travel freely through the universe. For these reasons, gravitational waves can be used to detect sources which are invisible by other means: binaries of compact objects such as black holes (BH) and neutron stars (NS), events such as supernovae and also processes of the early universe.

This project is dedicated to modelling the gravitational signal from merging black holes, more concretely to the phenomenon of *spin precession*. Mathematical models of the signal are indispensable for the detection of gravitational waves. Models are compared with detector data in order to detect weak signals, but even more importantly they are necessary to identify the origin of detected gravitational wave events, and to measure the parameters of the sources, such as their masses, spins, or distance. When the spins (angular momenta of the individual black holes) are orthogonal to the orbital plane, this plane is preserved. We will however be interested in the general case, when the spin of one or both components of the binary is not perpendicular to the orbital plane. Spin-orbit and spin-spin couplings then induce the orbital plane, and the spin vectors themselves, to exhibit a complicated precessing motion. The spin precession is thus related to a breaking of the symmetries of the system. In order to describe precessing systems, it has turned out to be fruitful to use a (non-inertial) co-precessing frame in which the decomposed waveform is similar to a non-precessing one. The description of this non-inertial frame requires the definition of a time dependent rotation between the inertial and non-inertial frames, which is usually described in terms of Euler angles. The main objective of this project is to study the quaternion description of these rotations in comparison with the Euler angle description, and investigate whether waveform models previously developed within the UIB group should be modified to adopt the quaternion description.

1.1   Gravitational waves

Gravitational waves are transverse waves that travel at the speed of light, caused by energetic and violent processes which distort spacetime. They propagate in all directions from the source as ripples of spacetime that carry information about the process and also about the nature of gravity. Any massive object that accelerates in a way which changes its quadrupole moment produces gravitational waves, but only those sources which are sufficiently massive generate waves detectable for our instruments. The most efficient way to accelerate masses is in binary systems, and indeed all gravitational wave signals detected so far have been produced by the coalescence of compact binaries. In addition, the more compact and heavy the source, the easier it will be to detect its gravitational waves, and therefore black hole binaries, where objects of several solar masses are accelerated to significant fractions of the speed of light within small regions of spacetime at most several hundred kilometers across, are the most detected so far [2]. The kind of gravitational waves produced by such sources are known as Compact Binary Coalescence (CBC). As we will see below, CBC signals are short transient signals. Other types of signal are

intensively searched for, but have not yet been detected, such as the continuous waves emitted by deformed spinning neutron stars [4], or the stochastic signals that may have been generated during the first fractions of a second of expansion of the universe [5].

The first direct gravitational wave detection was made by the Advanced Laser Interferometer Gravitational-Waves Observatory (LIGO) on September 14, 2015 [1]. The signal was found to be produced by a black hole binary of initial masses of $36^{+5}_{-4}M_\odot$ and $29^{+4}_{-4}M_\odot$. Three observation "runs" (O1, O2, O3) have so far been carried out with the advanced generation of interferometric GW detectors. Between observation runs, the detectors have been upgraded and their sensitivity increased further. The third observation run has recently been suspended on March 26 2020 [6], roughly a month before the planned end, due to the COVID-19 pandemic. While in O1 and O2 the LIGO-Virgo collaboration has confidently detected 11 GW events [2], already 56 detection candidates from this run have been publicly announced on `gracedb.ligo.org`. The next observation run, O4, is planned to start in late 2021 and reach the planned design sensitivity of the detectors. Further detector upgrades after O4 are already scheduled.

As stated, most of the observations have been from BH mergers, but a first binary NS merger has also been detected on August 17, 2017 [7]. Furthermore, possible candidates for NS-BH mergers have been identified (see the `gracedb.ligo.org` public announcement system). LIGO has played a role in all detections to date, with the Virgo detector joining during the second observation run. Additionally, on 25 February 2020 Kamioka Gravitational Wave Detector (KAGRA) [8] in Japan became operational, which will improve the detection and localization of future gravitational wave signals. The first space-based detector, LISA [9], is scheduled to fly and will be able to detect phenomena much more massive than the ground-based detectors, such as mergers of the supermassive black holes typically found at the centers of galaxies.

Even though the first gravitational-wave direct detection happened in 2015, their existence was predicted by Albert Einstein in 1916 [3], a year after his publication of the theory of General Relativity [10]. General Relativity arises from including gravity in the theory of Special Relativity, and understanding it not as a force, but as a geometric property of spacetime. In this theory particles move along geodesics, which is the generalization of a straight line in a curved space. That curvature is due to the energy or momentum of matter or radiation, and the relation between these properties is established by the Einstein field equations (EFE),

$$R_{ab} - \frac{1}{2}Rg_{ab} = \frac{8\pi G}{c^4}T_{ab}, \tag{1.1}$$

where R_{ab} is the Ricci curvature tensor, R is the scalar curvature, g_{ab} is the metric tensor, G is Newton's gravitational constant, c the speed of light in vacuum and finally T_{ab} is the stress-energy tensor. The Ricci tensor or curvature can be obtained as a contraction of the Riemann tensor, which is a combination of derivatives of the Christoffel coefficients:

$$R_{ab} = R^c{}_{acb} = \frac{\partial \Gamma^c{}_{ab}}{\partial x^c} - \frac{\partial \Gamma^c{}_{ac}}{\partial x^b} + \Gamma^c{}_{ab}\Gamma^d{}_{cd} - \Gamma^c{}_{ad}\Gamma^d{}_{bc}, \tag{1.2}$$

where the quantities $\Gamma^a{}_{bc}$ are the Christoffel symbols,

$$\Gamma^a{}_{bc} = \frac{g^{ad}}{2}\left(\frac{\partial g_{db}}{\partial x^c} + \frac{\partial g_{dc}}{\partial x^b} - \frac{\partial g_{bc}}{\partial x^d}\right). \tag{1.3}$$

Finally, the scalar curvature R is the trace of the Ricci curvature tensor, $R = g^{ab}R_{ab} = R^a_a$.

The EFE (1.1) are simple as tensor equations but very complex when written as partial differential equations for the metric components. It is these equations which predict phenomena such as gravitational waves (GWs), black holes (BHs), and the expansion of the universe. When the stress-energy tensor T_{ab} is zero in the region under consideration, the EFE are referred to as vacuum field equations or vacuum Einstein equations: $R_{ab} = 0$.

1.1.1 Linearized Einstein equations: gravitational waves

The most natural starting point for discussions of GWs is linearized gravity. For spacetimes whose geometries differ slightly from flat spacetime, it is possible to solve analytically the vacuum Einstein equations, which comprise ten nonlinear, partial differential equations for the ten metric coefficients g_{ab}. Linearized gravity is an approximation to general relativity when the spacetime metric $g_{ab}(x)$ is treated as a small deviation of the metric from flat spacetime η_{ab}, which in inertial Cartesian coordinates (t, x, y, z) can be written in the simple form $\eta_{ab} = diag(-1, 1, 1, 1)$. Metrics for this kind of spacetime can be written as

$$g_{ab}(x) = \eta_{ab} + h_{ab}(x), \ |h_{ab}| \ll 1, \tag{1.4}$$

where h_{ab} is the metric perturbation, which is assumed to be weak, and the coordinate system to be approximately Cartesian and inertial. Furthermore, terms of higher order than linear in h_{ab} will be neglected in all the expressions.

In order to obtain the linearized Einstein equations we must insert Eq. (1.4) into $R_{ab} = 0$ and expand it to first order in $h_{ab}(x)$. Two terms are obtained in this expansion, the first one is the Ricci curvature of flat spacetime, which vanishes, and the second term is the linearized equation we are looking for. Substituting Eq. (1.4) into Eq. (1.3), we can obtain the first-order perturbation terms of the Christoffel symbols, since the zeroth order vanishes because the components of η_{ab} are constant:

$$\delta\Gamma^c_{ab} = \frac{1}{2}\eta^{cd}\left(\frac{\partial h_{da}}{\partial x^b} + \frac{\partial h_{db}}{\partial x^a} - \frac{\partial h_{ab}}{\partial x^d}\right). \tag{1.5}$$

The perturbation in the Ricci curvature can be found by inserting Eq. (1.5) into Eq. (1.2), taking into account that the last two terms do not contribute since they are of second order in h_{ab}. The perturbation of the Ricci tensor then becomes

$$\delta R_{ab} = \frac{\partial\delta\Gamma^c_{ab}}{\partial x^c} - \frac{\partial\delta\Gamma^c_{ac}}{\partial x^b}. \tag{1.6}$$

Finally, the linearized vacuum EFEs are obtained by substituting Eq. (1.5) into Eq. (1.6)

$$\delta R_{ab} = \frac{1}{2}[-\Box h_{ab} + \partial_a V_b + \partial_b V_a] = 0, \tag{1.7}$$

where $\Box = \eta^{ab}\partial_a\partial_b$ is the flat-space wave operator (d'Alembertian) and the vector V_a is defined as $V_a = \partial_c h^c_a - \frac{1}{2}\partial_a h^c_c$, where $h^c_a = \eta^{cd}h_{da}$: indices on perturbations can be raised and lowered with the flat space metric. The equation (1.7) is a set of ten linear, partial differential equations for $h_{ab}(x)$. As coordinates are arbitrary, a specific choice can simplify the solutions, but it has to leave the components of η_{ab} unchanged. Let us consider the following change:

$$x'^a = x^a + \xi^a(x), \tag{1.8}$$

where $\xi^a(x)$ are four arbitrary functions of the same small size as $h_{ab}(x)$. This change of coordinates implies a metric transformation

$$g'_{ab}(x') = \frac{\partial x^c}{\partial x'^a}\frac{\partial x^d}{\partial x'^b}g_{cd}(x) = \eta_{ab} + h'_{ab} = \eta_{ab} + (h_{ab} - \partial_a\xi_b - \partial_b\xi_a). \qquad (1.9)$$

Adding a term $\partial_a\xi_b + \partial_b\xi_a$ to the metric perturbation thus corresponds to a coordinate transformation rather, and is physically equivalent. This *gauge transformation* is analogous to $A_a \to A_b + \partial_a\Lambda$ for the vector potential in electromagnetism. Since $\xi^a(x)$ are arbitrary functions, they can be chosen so that $V'_a(x) = 0$, called the *harmonic gauge conditions* In fact, it can be assumed that the initial coordinate system already satisfies $V_a(x) = 0$, simplifying the linearized Einstein equation to

$$\Box h_{ab} = 0. \qquad (1.10)$$

Just as in electromagnetism, Eq. (1.10) admits the solution of a superposition of plane waves, *gravitational waves*, which propagate at the speed of light

$$h_{ab}(x) = a_{ab}e^{i\mathbf{k}\cdot\mathbf{x}}, \qquad (1.11)$$

where a_{ab} is a symmetric 4×4 matrix which gives the amplitudes of the components of the wave, which are not arbitrary and can be simplified by choosing an appropriate set of coordinates. Explicit calculations show that the metric perturbation is purely spatial ($h_{ti} = 0$) and traceless ($h^a_a = 0$). In addition, the harmonic gauge condition implies that the spatial metric perturbation is transverse, just as are electromagnetic waves, $k^i a_{ti} = \partial_a h_{ab} = 0$ and also that $a_{tt} = 0$: this is called the *transverse-traceless (TT) gauge*, which fixes the local gauge freedom. Orienting the z-axis along the propagation of the wave, all that is left is a 2×2 symmetric and traceless matrix in the x-y subspace, which exhibits the fact that gravitational waves have only two polarizations, i.e. local degrees of freedom, called h_+ and $h_\times$:

$$h_{ab}(x) = \begin{bmatrix} 0 & 0 & 0 & 0 \\ 0 & h_+ & h_\times & 0 \\ 0 & h_\times & -h_+ & 0 \\ 0 & 0 & 0 & 0 \end{bmatrix} e^{i\mathbf{k}\cdot\mathbf{x}}. \qquad (1.12)$$

1.1.2 Gravitational waves from black hole binaries

A few months after the publication of general relativity, Karl Schwarzschild found a solution to the spherically symmetric and stationary vacuum solution of the Einstein field equations [11]. This solution becomes singular at what is called the Schwarzschild radius, and although it was not understood at the time, that surface is the event horizon: causal influences can cross it in only one direction. That is the definition of a black hole, it is a region of space-time where neither matter nor radiation can escape, whose boundary is called the event horizon. A known formation channel for black holes is the gravitational collapse of stars, which occurs when the star's internal pressure cannot resist its own gravity. The remnant mass after the collapse determines which type of compact star results from the process. If this mass is high enough that even the neutron degeneracy pressure cannot stop the collapse, the object inevitably becomes a black hole.

Black hole binary (BHB) mergers are key sources for gravitational-wave astronomy. Only accelerating masses can generate gravitational waves and a particularly effective

way to accelerate astrophysical objects is through orbital motion. As the distance between objects decreases, the frequency increases, consequently binaries are more effective to produce gravitational waves when they are closer. Since black holes are the most compact astrophysical bodies, and thus can orbit at the smallest separations and highest frequencies, BHB are the most effective known source of gravitational waves. As we will see below, the frequency is indirectly proportional to the total mass, and so the frequency band of a detector determines the masses of binary systems that can be observed.

The no-hair theorem [12], [13] states that a stationary black hole solution is completely described by only three parameters: the mass, the charge and the angular momentum. Astrophysical bodies, like stars, do not have charge since their intense electromagnetic field would expel it. Thus, astrophysical black holes are also not expected to have charge, but will in general be rotating; the corresponding equilibrium solution was found by Kerr in 1963 [14]. Hence, rotating black holes without charge are referred to as Kerr black holes, and are characterized by their spin angular momentum (**S**) and mass. Therefore, the parameter space of a binary is composed by two masses and two spins (8 parameters). If the orbit is circular, there are no further parameters, since the separation between the two masses then determines the velocity. For eccentric orbits two more parameters are needed to characterize the orbit (the eccentricity and the orientation of the ellipse). However, eccentric orbits are expected to be rare, since they tend to circularize rapidly in the absence of other interactions [15], so current data analysis efforts focus on circular binaries. It is convenient to use geometrized units $G = c = 1$, so in vacuum general relativity, where other fundamental constants are absent, the mass acts simply as a scale parameter. The parameter space is then the mass ratio $q = m_1/m_2 \geq 1$ and both spins of the black holes.

The coalescence of black hole binaries has three phases. The inspiral is the process in which a pair of compact objects revolve around each other during millions of years, emitting GWs that carry away orbital energy from the system. This loss of energy diminishes the orbit and increases the frequency, hence loosing more energy with stronger GWs. This process ends with the merger of both objects and the following ringdown of the resulting compact object. In this last stage, the remnant BH oscillates, emitting GWs until it settles down to a Kerr BH. Analytic approximation techniques can provide a good qualitative description of the gravitational wave signal. The simplest version of these calculations is based on Newtonian orbital dynamics (Kepler's third law) and Einstein's quadrupole formula (for a textbook development see e.g. [16] ch. 4.1), which yields the following results for the gravitational wave strain polarizations, establishing the z-axis orthogonal to the orbital plane

$$h_+(t) = \frac{4G\mu\omega_s^2 R^2}{rc^4} \frac{1+\cos^2(\theta)}{2} \cos(2\omega_s t), \quad h_x(t) = \frac{4G\mu\omega_s^2 R^2}{rc^4} \cos(\theta)\sin(2\omega_s t), \quad (1.13)$$

where R is the separation between both objects, r the distance to the system, η the reduced mass and ω_s the orbital frequency. These expressions show that radiation has a frequency of twice the orbital frequency ($\omega_{GW} = 2\omega_s$). Further development provides expressions for the evolution of the GW frequency in time:

$$f_{GW}(t) = \frac{1}{\pi} \left(\frac{5}{256(t_{coal} - t)} \right)^{3/8} \left(\frac{GM_c}{c^3} \right)^{-5/8}, \quad \tau = \frac{5}{256}(\pi f_{GW})^{-8/3} \left(\frac{GM_c}{c^3} \right)^{-5/3}, \quad (1.14)$$

where M_c is the chirp mass $M_c = M \left(\frac{q}{(1+q)^2} \right)^{3/5}$, M is the total mass of the binary, t_{coal} is the coalescence time starting at a reference time and τ is the time until coalescence for a

certain frequency ($\tau = t_{coal} - t$). The radiation power emitted during the process is given by

$$P = \frac{32c^5}{5G}\left(\frac{GM_c\omega_{GW}}{2c^3}\right)^{10/3}. \tag{1.15}$$

During the inspiral, the amplitude of the emitted waves increases as both objects come closer. The signal becomes detectable when the compact objects orbit fast enough, and the peak amplitude occurs at the merger. During the ringdown to the remnant Kerr black hole the amplitude decays exponentially and quickly becomes undetectable. The time the system is emitting detectable GWs depends on the masses of the objects involved. Let us consider two equal mass systems, a neutron star ($M_{NS} = 3M_\odot$) binary and a black hole ($M_{BH} = 50M_\odot$) binary. The minimum frequency which can be detected with LIGO at design sensitivity is approximately 10 Hz, which implies (using Eq. (1.14)) $\tau_{NSB} \approx 15$ minutes and $\tau_{BHB} \approx 8$ seconds: a signal coming from a binary of massive black holes can last several seconds, while from a neutron star merger, hundreds of seconds.

Although these approximations give qualitatively correct results during the inspiral, they are not sufficiently accurate for gravitational wave data analysis. A more accurate description of the inspiral can be obtained from the Post-Newtonian (PN) expansion [17], which expresses deviations from the approximations corresponding to equations 1.13 and 1.15 in terms of an expansion in the parameter v^2/c^2. For strong fields and velocities close to the speed of light, as occurs when the black holes come close, the expansion breaks down. For the last orbits and the merger, perturbative methods can not be used, and the Einstein equations need to be solved numerically with the methods of numerical relativity. Complete descriptions of the gravitational wave signal from compact binaries thus have only been possible since breakthroughs in numerical simulations in 2005 [18]–[20].

Numerical simulations can only produce waveforms for discrete points on the parameter space, building up catalogs. Accurate descriptions of gravitational wave signals from black hole binaries can be developed by calibrating theoretical models to catalogs of numerical relativity simulations. A large international effort is underway to further develop such waveform models, and the underlying analytical and numerical frameworks to describe the relativistic two-body dynamics. The two major families of such models are the time-domain effective-one-body (EOB) models, which are based on "deforming" post-Newtonian Hamiltonians and energy fluxes (see e.g. [21]) and the frequency domain phenomenological models partially developed at UIB (see e.g. [22]–[25]). Since frequency domain templates are needed to compute the scalar product with detector data, models were first constructed in the Fourier domain. These models then achieve fast evaluation times in data analysis procedures. However, the time domain description of the signal provides the dynamical information of the source in a more direct way, and also insights to develop strategies for modelling binary systems.

1.2 Gravitational wave data analysis and waveform modelling

Gravitational wave detectors are essentially Michelson interferometers, which measure the gravitational wave strain as a difference in the length of their arms. This difference leads to an interference phase of the beams emitted by each arm, which transmits an optical signal proportional to the strain of the wave. A basic scheme of its operation and images of both LIGO detectors can be seen in Figure 1. In order to achieve the required sensitivity to detect gravitational waves, great effort is needed to reduce seismic and thermal noise, other noise sources and optical phase fluctuations. The sum of all noise contributions leads to the sensitivity curve of the detector as a function of frequency, shown in Figure 2.

1.1: Aereal views of the the LIGO Hanford and LIGO Livingston interferometers.
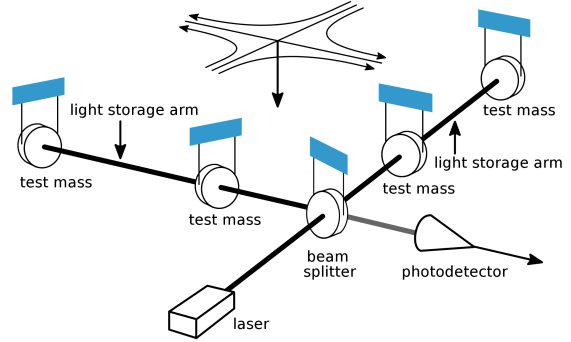
1.2: Basic schematic of LIGO's interferometers (Caltech/MIT/LIGO Lab).
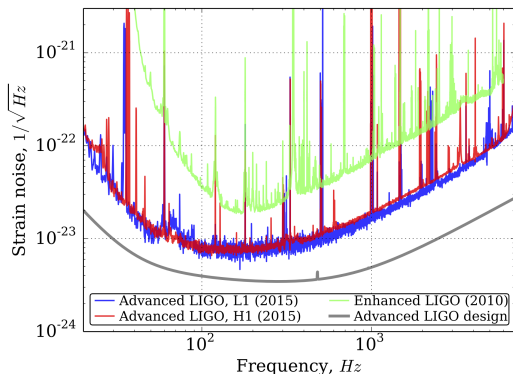
Figure 1: Images recovered from LIGO Caltech.

Figure 2: Spectral amplitude of the total strain noise in units of strain per $\sqrt{Hz}$. Image recovered from [26].

This picture shows the sensitivity of the Advanced LIGO detectors in the first observation run (O1) (September 2015-January 2016), which was about a factor of three to five better than the instruments in 2010 in their most sensitive band, while at lower frequencies the improvement is more than ten times better. The sensitivity of the detector is limited at low and high frequencies, and the most sensitive frequency band is between 100 Hz and 300 Hz.

Thus, in the output data $d(t)$ of any real detector there will be the GW signal $s(t)$ and also the detector noise $n(t)$, so $d(t) = s(t) + n(t)$. The *noise spectral density* $S_n(f)$ is defined so that the ensemble average over different noise realizations of $n^2(t)$, $\langle n^2(t)\rangle$, is obtained integrating this function over the physical range of frequencies,

$$\langle n^2(t)\rangle = \langle n^2(0)\rangle = \int_{-\infty}^{\infty} df\ df'\langle n^*(f)n(f')\rangle = \int_0^{\infty} df\, S_n(f). \qquad (1.16)$$

If $n(t)$ is dimensionless, $S_n(f)$ has dimensions Hz^{-1}. The noise of the detector then can be characterized by $\sqrt{S_n(f)}$, which is called *spectral amplitude* (see Figure 2).

The noise of real detectors is typically considered as a superposition of Gaussian noise and non-Gaussian artefacts usually referred to as "glitches". For stationary Gaussian noise one can assume without loss of generality that $\langle n(t)\rangle = 0$. Most importantly, for stationary Gaussian noise there exists an optimal method of detection when the possible signals can be predicted theoretically: this method is matched-filtering [27] (for a textbook development see e.g. [16] ch. 7) with accurate templates. The main idea of this method is to compute the scalar product between the output of the detector $d(t)$ and the template $h(t)$, chosen such that it maximizes the signal-to-noise ratio (SNR). Defining the scalar product between two real variables as

$$\langle A(t)|B(t)\rangle = 4 \cdot \mathrm{Re} \int_0^{\infty} df\, \frac{\tilde{A}^*(f)\tilde{B}(f)}{S_n(f)}, \qquad (1.17)$$

11

the SNR can be defined as S/N, where S is the expected value of a quantity which depends on the output of the detector and the template and N is its RMS value when the signal is absent. Applying the SNR definition to the scalar product then implies

$$\frac{S}{N} = \frac{\langle(d|h)\rangle}{\sqrt{\langle(n|h)\rangle\langle(h|n)\rangle}} = \frac{(s|h)}{\sqrt{(h|h)}}, \tag{1.18}$$

where the second equality is obtained by evaluating the ensemble averages over noise realizations [28]. The SNR optimal value is $\sqrt{(h|h)}$, so it becomes

$$\text{SNR}_{opt}^2 = \left(\frac{S}{N}\right)_{opt}^2 = 4\int_0^\infty df \frac{|\tilde{h}(f)|^2}{S_n(f)}. \tag{1.19}$$

For Gaussian noise, the optimal search strategy is to optimize the SNR over the templates h. A detection then corresponds to statistically significant peaks in the SNR, when compared with a suitably computed background, and taking into account a χ^2 test, see e.g. [1], [29], [30].

Data analysis then proceeds in two steps: First, "searches" are performed (see e.g. [30]), which aim to deliver statistically significant detections and which are optimized to maximize the detection rate while minimizing the false alarm rate. Once a detection is made, a more detailed analysis called "parameter estimation" is performed [31], which uses the methods of Bayesian inference to measure the source parameters: the intrinsic parameters (masses and spins) and the extrinsic parameters (sky location, distance, inclination, polarization and coalescence phase) and compute error estimates.

There are different ways to perform searches, which generally rank events according to an appropriate detection statistic. This value quantifies the SNR of the event and the consistency of the data between both detectors. Generic transient searches operate without a specific waveform model and classify events based on their amplitude and the evolution of the frequency in time. Such generic searches allow to discover unmodelled signals. Matched filter binary coalescence searches on the other hand are dedicated directly to the detection of gravitational waves from a binary. The search calculates the matched-filter signal-to-noise ratio (1.19) and identifies its maximum in time and within a template bank of possible signals. For reasons of computational efficiency, matched-filter searches only provide an approximate estimation of the source parameters, so the more detailed follow-up analysis of parameter estimation is needed to determine the features of the source. While several 10^5 templates are typically used for binary coalescence searches, approximately $10^7 - 10^9$ models based on general relativity are used for parameter estimation. Bayesian inference then provides a probability distribution of the source parameters obtained, which allows to determine the spins and masses of both initial black holes and the final object, the distance of the source and also the total energy radiated in gravitational waves.

Therefore, waveform modelling is important to provide templates for the detection of weak signals, but it becomes indispensable for parameter estimation and thus to understand the origin of events. Waveforms analyzed in this project are those coming from systems with misaligned spins, which exhibit a phenomenon known as *spin precession*.

1.3   Precessing systems

For a binary composed of two rotating black holes whose spin vectors $(\mathbf{S_1}, \mathbf{S_2})$ are orthogonal to the orbital plane and thus parallel or anti-parallel to the orbital angular

momentum (**L**), there exists an equatorial symmetry of the spacetime with respect to the orbital plane. This symmetry is preserved in time, and so are the orbital plane and the directions of the spins. Therefore, the intrinsic parameter space for these systems is four dimensional, since only two parameters are needed for the spin components orthogonal to the orbital plane and two more for the masses. Introducing the mass ratio q and recalling that the total mass serves as a scale parameter, then the parameter space that needs to be modelled becomes three dimensional. These systems are referred to as non-precessing. In this case the change of total angular momentum $\mathbf{J} = \mathbf{L} + \mathbf{S_1} + \mathbf{S_2}$ is due to the emission of gravitational waves. Note that only the orbital angular momentum **L** will change significantly, since the individual bodies are sufficiently axisymmetric and thus do not emit gravitational radiation on their own. Furthermore, due to their compactness it turns out that they absorb very little gravitational wave energy and angular momentum.
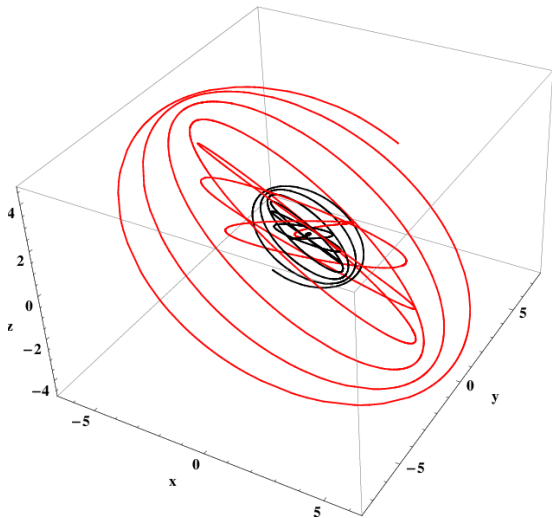

Figure 3: Trajectories of the smaller (red) and larger (black) BHs for a precessing simulation at $q = 3$. Image taken from [32].

Precessing systems are characterized by the spin of one or both black holes not being orthogonal to the orbital plane. This situation leads to a variation of **S** and **L** in time; hence, the orbital plane inclines and precesses also over time. An example of a precessing binary motion is shown in Figure 3. In this more general case, the parameter space is that of eight parameters. The main effect of precession on the waveform is an amplitude modulation resulting from the time dependence of the orthogonal direction to the orbital plane, which is the dominant direction in which gravitational waves are radiated. This modulation complicates the production of analytic precessing-binary waveforms and it is necessary to define an appropriate frame in which to describe the data analytically.

The evolution of coalescing binary systems can be studied using a post-Newtonian (PN) approximation [17]. Since during the last stage of the binary the velocity is not expected to be small, high order expansions are desirable, and the highest available order for different quantities has been slowly increasing during the last decades, with many quantities available at 3PN, i.e. $(v/c)^6$, or 4PN order. The spins of both black holes play an important role in the orbital dynamics and gravitational wave emission. At low order (sufficiently low frequency), the spin effects have two contributions, one due to the spin-orbit (SO) interaction and the other due to the spin-spin (SS) interaction (for a discussion of both terms, see e.g. [33] or [21]).

The post-Newtonian equations of motion can be obtained from a Hamiltonian. In order to discuss the qualitative nature of spin effects we will focus on the leading order spin-orbit Hamiltonian, which reads

$$H_{SO} = 2\frac{\mathbf{S_{eff}} \cdot \mathbf{L}}{R^3}, \tag{1.20}$$

where R is the separation between the black holes and the effective spin $\mathbf{S_{eff}}$ is defined as

$$\mathbf{S_{eff}} = \left(1 + \frac{3}{4}\frac{m_2}{m_1}\mathbf{S_1}\right) + \left(1 + \frac{3}{4}\frac{m_1}{m_2}\mathbf{S_2}\right). \tag{1.21}$$

Equation (1.20) implies that the potential energy depends only on the parallel component of the spin to the orbital angular momentum. One can see from the sign of (1.20) that the interaction between bodies will be attractive or repulsive if $\mathbf{L}$ and $\mathbf{S}$ are anti-aligned or aligned, respectively. If the interaction is attractive, then the compact objects will inspiral together faster, while in case of having a positive Hamiltonian, the inspiral will take longer, radiating more gravitational waves. From the spin-orbit interaction, one can also derive the PN evolution equation for the black hole total spin

$$\dot{\mathbf{S}} = -\frac{2}{R^3}\mathbf{S_{eff}} \times \mathbf{L}. \tag{1.22}$$

This last equation shows that the spin will be preserved if the effective spin is parallel to the orbital angular momentum, such as it happens for non precessing binaries. However, if the cross product between both vectors does not vanish, then the spin evolves, producing a precession of the orbital plane and therefore a modulation of the waveform. This precession depends on the orbital angular momentum $\mathbf{L}$, the total spin $\mathbf{S}$ and their relative orientations. If the angle between both vectors is small, so will be the modulation, and if the module of $\mathbf{S}$ is much smaller than $\mathbf{L}$, the modulations can be neglected. Thus, the orthogonal components of $\mathbf{S}$ are relevant neither for the speed at which the inspiral binaries together nor for the amount of gravitational waves radiated, but only for the orbital plane and spin precession.

To leading PN order one can split the orbital angular momentum as [33]

$$\mathbf{L} = \mathbf{L_N} + \mathbf{L_{PN}} + \mathbf{L_{SO}}, \tag{1.23}$$

where $\mathbf{L_N} = \mu(\mathbf{r} \times \mathbf{v})$ is the Newtonian orbital angular momentum, and the other terms are

$$\mathbf{L_{PN}} = \mathbf{L_N}\left[\frac{1}{2}v^2(1-3\eta) + (3+\eta)\frac{M}{r}\right],$$
$$\mathbf{L_{SO}} = \frac{\mu}{M}\left[\frac{M}{r}\mathbf{n} \times \left(\mathbf{n} \times \left(3\mathbf{S} + \delta M\left(\frac{\mathbf{S_1}}{M_2} - \frac{\mathbf{S_2}}{M_1}\right)\right)\right) - \frac{1}{2}\mathbf{v} \times \left(\mathbf{S} + \delta M\left(\frac{\mathbf{S_1}}{M_2} - \frac{\mathbf{S_2}}{M_1}\right)\right)\right]. \tag{1.24}$$

The evolution of the orbital angular momentum up to 2PN order is [34]

$$\begin{aligned}\dot{\mathbf{L}} = &\left[\left(2 + \frac{3}{2}q\right) - \frac{3}{2}\frac{v}{\eta}\left[(\mathbf{S_2} + q\mathbf{S_1}) \cdot \hat{\mathbf{L}}\right]\right]v^6(\mathbf{S_1} \times \hat{\mathbf{L}}) \\ &+ \left[\left(2 + \frac{3}{2q}\right) - \frac{3}{2}\frac{v}{\eta}\left[(\mathbf{S_1} + \frac{1}{q}\mathbf{S_2}) \cdot \hat{\mathbf{L}}\right]\right]v^6(\mathbf{S_2} \times \hat{\mathbf{L}}) \\ &+ \mathcal{O}(v^7),\end{aligned} \tag{1.25}$$

where $\eta = q/(1+q^2)$ is the symmetric mass ratio. The addition of these terms to the equations of motion has important implications for the binary evolution and thus for the waveform (see Fig. 3).

The development of precessing waveform models has proven difficult: the complexity of precession makes it difficult to solve the PN equations at high order and to develop phenomenological descriptions, while the large dimensionality of the parameter space makes it difficult to sample it with numerical relativity simulations. In order to simplify the problem it has turned out to be fruitful to work in coordinate frames that are adapted to the precessing motion, and which are rotated relative to a fixed inertial frame. The discussion of gravitational waves from precessing systems, and the role of frame rotations will be the subject of the next section.

2 Gravitational waves from precessing systems

2.1 Spherical harmonic decomposition

In order to determine the gravitational wave signal, it is common to combine the transverse-traceless projections of the strain, introduced in Section 1.1.1, Eq. (1.12), into a single complex quantity $h(t, \mathbf{r}) = h_+(t, \mathbf{r}) - ih_\times(t, \mathbf{r})$. At large distance (as is the case in astronomy) the strain is inversely proportional to the distance, i.e.

$$h(t, \mathbf{r}) = \frac{h_0(t, \hat{\mathbf{r}})}{r} + O(r^{-2})$$

and one is only interested in the quantity h_0. Similar as for other radiation problems, it is useful to describe the angular dependence by spherical harmonics. The strain, which is a tensorial quantity, can be expanded in terms of spin-weighted spherical harmonics (SWSHs) with spin weight $s = -2$ [35],

$$h(t, \mathbf{r}) = \frac{1}{r} \sum_{l \geq 2, m=-l}^{m=l} h^{l,m}(t) Y_{l,m}^{-2}(\hat{\mathbf{r}}) = \frac{1}{r} \sum_{l,m} h^{l,m}(t) Y_{l,m}^{-2}(\theta, \phi), \tag{2.1}$$

where (θ, ϕ) are the standard polar coordinates on the unit sphere. Given this relation, it is useful to discuss directly the modes $h^{l,m}(t)$ instead of the function value in any particular direction. Higher order terms are strongly suppressed, and for comparable mass systems only a handful of terms are required for current data analysis applications [24]. This representation of the waveform in terms of a few functions that only depend on time, instead of a single function that depends on time and two angles is significantly simpler.

First-order calculations based on Newtonian orbital dynamics and Einstein's quadrupole formula (see Eq. (1.13)) show that non-precessing binary systems predominantly emit gravitational waves in the direction of $\theta = 0, \pi$, i.e. orthogonal to the orbital plane, which for those systems corresponds to the direction of the orbital angular momentum $\mathbf{L}$. Consistent with the symmetry of such systems, it is natural to orient the z-axis in this direction. It then turns out that there exists a natural hierarchy of mode amplitude, with modes with a smaller value of $|m|$ having smaller amplitude. The dominant modes are then those given by the $(l = 2, m = |2|)$ spherical harmonics of the wave. The modes $|m| = 1$ vanish if the two black holes can be exchanged by symmetry and $m = 0$ is a non-oscillating mode which is related to memory effects, see e.g. [36]. There are some other features of the modes of non-precessing systems that yield simplifications. For example, the invariance of the system under reflection across the orbital plane (generally x-y plane) is expressed by (deduction in Appendix C of [37]):

$$h^{l,m} = (-1)^l \, (h^{l,-m})^* \tag{2.2}$$

being h^* the complex conjugate. One can thus restrict to analyzing modes with negative values of m, since the complex amplitudes of the two modes $(l, \pm m)$ are equal but differ on their complex phases up to an addition of π for old l. Furthermore, during the inspiral a simple relation holds to high accuracy between the modes and the orbital phase Φ,

$$h^{l,m} \propto e^{-im\Phi}. \tag{2.3}$$

If the system is rotated, the modes with the same index l are mixed, and hence, the description of gravitational waves with SWSHs becomes complicated. For precessing

systems no natural fixed z-axis can be chosen, and consequently the natural amplitude hierarchy for each l is lost. Likewise the symmetry property of Eq. (2.2) and the relation of Eq. (2.3) do not hold for precessing systems. Both failures in these equations for precessing binaries are not just because of the mode mixing in a fixed basis, but also will appear in any frame.

2.2 Quadrupole aligned frame

A breakthrough idea in modelling precessing systems has been to find a co-precessing frame in which Eq. (2.3) becomes approximately true [32]. The search of the preferred frame in which to describe the data analytically implies the use of geometrical methods to determine a new basis in which to express gravitational wave modes.

Non-precessing systems can be characterized by two time scales, the time scale of the approximately circular orbital motion, and the inspiral time scale of the radial motion, which is much slower. Precessing systems show a third time scale, of the precessing motion, which lies in between the orbital and inspiral time scales. Consequently, the acceleration is much larger due to the orbital motion than due the precessing or radial motion. Since the emission of gravitational waves is due to acceleration, the orbital motion dominates the radiated power, and neglecting the power emitted due to the radial and precessing motion is a good approximation in the inspiral. The inspiral rate of a precessing system is thus well approximated by that of a non-precessing system.

These ideas lead to considering an approximate map between precessing and non-precessing waveforms [32]: in an appropriately co-rotating frame (which is thus non-inertial) the waveform should look similar to a non-precessing waveform. Mapping a non-precessing waveform to a precessing one in this way is usually referred to as "twisting up" the non-precessing signal [22].

It turns out [32] that the mode structure of precessing waveforms in an appropriate co-rotating frame is indeed very similar to that of a corresponding non-precessing wave-form. Moreover, post-Newtonian approximations permit to compute the time dependent rotation from the co-rotating frame, where the precessing waveform is approximated by a non-precessing one, to the inertial frame, in which gravitational wave data analysis is performed (e.g. the frame of the source or the detector) [22]. Hence, the fact that the twisting up procedure can be performed using PN expansions has given rise to a variety of phenomenological waveform models for precessing waveforms, starting with [22]. These models have become standard tools in gravitational wave astronomy, in particular the frequency domain PhenomP [22] and PhenomPv2 models [23] and also the time domain IRMPhenomTP [38], which have been implemented in the open source LIGO Algorithm Library (LAL) [39]. Their main idea is indeed the same: find a co-precessing frame (non-inertial) in which the decomposed waveform is similar to the one that is non-precessing, i.e. achieve a precessing waveform that can be approximated by rotating the one that would be produced for an aligned spin system. The description of this non-inertial frame needs the definition of a time dependent rotation between the vectors of the basis involved (inertial and non-inertial), which has been usually described using Euler angles (EA). Thus, it is necessary to find the new basis $Y_{l,m}^{s}(\theta', \phi')$ for the rotated system at each moment in time (with θ' and ϕ' being the rotated coordinates). However, using Euler angles has several disadvantages, since composing rotations in their terms is computationally expensive and can lead to inaccuracies due to sharp features and the phenomenon of gimbal lock discussed below. For this reason, in this project I investigate the quaternion representation of rotations.

Equation (2.1) transforms simply under rotations, which is essential to obtain the simplified waveform. Rotated modes $\widehat{h}^{l,m}$, which will be decomposed into an appropriate co-precessing frame, can be found using the relation

$$\widehat{h}^{l,m} = \sum_{m'} h^{l,m'} \mathcal{D}^{(l)}_{m',m}(R^{-1}), \tag{2.4}$$

where $\mathcal{D}^{(l)}_{m',m}$ is the Wigner matrix and R the rotation which transforms the first basis into the second one. Several techniques have been introduced to find a suitable frame in which to decompose the waveform, where the basis is not static anymore, but time dependent. The method used in this project to find the "co-precessing frame", described in [32], consists in locating the frame in which the decomposed waveform is similar to that of a non-precessing system. The dominant modes for these last systems are the $(l,m) = (2, \pm 2)$, called the quadrupole modes, and the purpose of this method is to find the non-inertial frame in which the amplitudes of these modes are maximized, denoted as the "quadrupole-aligned frame". The procedure consists in finding the direction of maximum gravitational radiation emission, which is perpendicular to the orbital plane. This direction is not exactly that of the orbital angular momentum as it is for non-spinning systems, but it is still a good approximation. However, when rotating the waveform, quadrupole modes mix up and aligning the rotating frame directly to the maximum emission direction is not sufficient, but it is necessary to impose another condition (Equation (2.6)). The method also produces higher-mode amplitudes consistent with those of non-precessing binaries, which is useful because those systems are better known. Thus, the main result is that the waveform can be represented in a simpler form which can simplify analytic models for precessing systems and also facilitate comparisons between numerical and analytic results.

The time dependent rotation between a fixed, i.e. inertial, frame and the quadrupole-aligned one is the main focus of this project. Unlike non-precessing systems, precessing binaries do not have a preferred inertial frame. However, there are some natural fixed frames which have benefit properties for the waveforms. The initial orbital angular momentum frame L_0 is usually used in numerical relativity waveforms. This frame has the property that the spin components are approximately conserved, i.e. perpendicular and parallel components of $\mathbf{S}$ do not change. For this reason, when rotating the waveform to the quadrupole frame, it will exhibit the same features as the one produced by a system with the same parallel components of $\mathbf{S}$. Another natural fixed frame is the one defined by the initial total angular momentum, the J_0 frame. Even though the L_0 frame permits an easier description of the spin components, the J_0 frame simplifies the initial waveform and hence, its manipulation to the rotated frame. Therefore, even if there is no preferred inertial frame for precessing systems, a smart choice of its coordinates can simplify the problem. Aligning the z-axis of the inertial frame in the chosen direction, the choice of the other axes is arbitrary, which can be made by imposing $\mathbf{L}$ to be in the x-z plane at some frequency of reference. The co-precessing frame requires to track the orbital plane, so the z'-axis is defined as $\mathbf{L}$, which is parametrized by the spherical angles (α, β) in the inertial frame (see Figure 4). The rotation freedom around that axis can also be fixed with an arbitrary election, and in this project we use the same convention as in [23], in particular $\mathbf{x}' = \mathbf{L_x}$.

The specification of the time-dependent rotation between the two triads (x, y, z) and (x', y', z') is usually defined by the Euler angles in the z_1-y'-z_2'' convention (intrinsic rotations, standard when using spherical harmonics), which implies a first rotation through an

angle α about the z-axis, then a second rotation about the y'-axis of angle β and finally, a third rotation ϕ around the new z''-axis. However, this is equivalent to rotations in the opposite order about fixed axes z_2-y-z_1 (extrinsic rotations), which is useful for calculations.
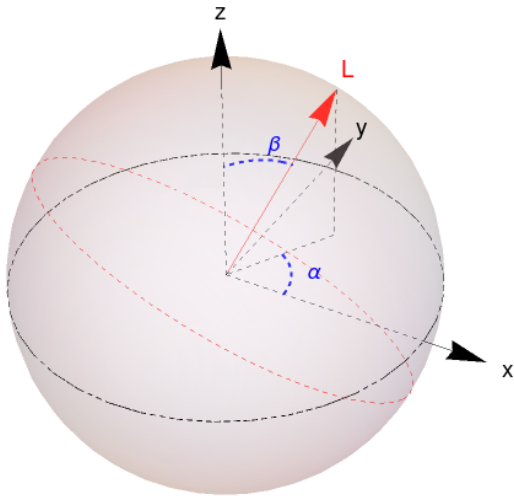

Figure 4: Definition of the Euler angles.

Euler angles form one set of coordinates for $\mathbb{SO}(3)$, the group of rotations of $\mathbb{R}^3$ about the origin. These rotations are described by orthogonal 3×3 matrices with positive unit determinant and the operation of the group is the composition of rotations. By construction, the first two Euler angles are given by α and β, which can be initially calculated as

$$\alpha = \arctan(L_y, L_x) = \arctan \frac{L_x}{L_y}, \qquad (2.5)$$
$$\cos \beta = \mathbf{z} \cdot \mathbf{L} = L_z.$$

The third angle can be found by imposing the minimal rotation condition, which is deduced in [40]:

$$\dot{\gamma} = -\dot{\alpha} \cos \beta. \qquad (2.6)$$

Equation (2.6) demands absence of rotation in the precessing frame about the orbital angular momentum. Hence, imposing this condition implies that waveforms decomposed in this new frame are invariant under rotations of the inertial frame and exhibit smoothly varying phase. Note that there exists a freedom in the angle γ, since this equation only specifies its derivative, and we can choose $\gamma = 0$ at the initial time or reference frequency (related by Eq (1.14)).

For the special case where z points in the $\mathbf{J}$ direction, denoted as J_0 frame, the evolution of the Euler angles can be obtained by introducing the triad $\mathbf{n}, \mathbf{L}, \boldsymbol{\lambda}$, where $\mathbf{n}$ is the unit separation vector between the black holes and $\boldsymbol{\lambda} = \mathbf{L} \times \mathbf{n}$. In this frame, we call the second Euler angle β_{JL}, while in the L_0 frame, it is denoted as ι. It can be shown [33] from post-Newtonian evolution equations that the total angular momentum is conserved at 2PN order when the loss of energy due to gravitational radiation is neglected. Thus, in this approximation the orbital angular momentum $\mathbf{L}$ must precess as $\dot{\mathbf{L}} = -\dot{\mathbf{S}}$, and the orbital angular momentum and total spin vectors precess around $\mathbf{J}$ on the slow precessional time scale. If the inspiral timescale is much greater than the orbital timescale, which holds until shortly before the merger, then radiation reaction changes the situation only slowly, changing the "opening angle" between $\mathbf{J}$ and $\mathbf{L}$. Hence, the Euler angles evolution equations are given by [25]

$$\dot{\alpha} = -\frac{\bar{\omega}}{\sin \beta_{JL}} \frac{J_n}{\sqrt{J_n^2 + J_\lambda^2}}, \qquad \dot{\beta_{JL}} = \frac{J_\lambda}{\sqrt{J_n^2 + J_\lambda^2}}, \qquad (2.7)$$

where $\bar{\omega}$ is the precession frequency for the orbital plane, defined as $\dot{\mathbf{L}} = -\bar{\omega}\boldsymbol{\lambda}$. Equations (2.7) and (2.6) are then solved next-to-next-to-leading order in the spin-orbit coupling, giving the evolution of the Euler angles in time, which give the rotation needed to obtain the quadrupole modes in this non-inertial frame [22].

The Wigner Matrices that appear in the expression of the rotated modes (Eq. (2.4)) form a representation of $\mathbb{SO}(3)$, and they can be expressed in terms of the Euler angles

as a convenient set of coordinates. An explicit expression for the Wigner Matrices and its derivation can be found in [41], which in our convention is given by

$$\mathcal{D}^{(l)}_{m',m}(\alpha, \beta, \gamma) = \sum_{k=\max[0,m-m']}^{\min[l+m,l-m']} \sqrt{(l+m)!(l-m)!(l+m')!(l-m')!}$$

$$\times e^{i(m'\gamma+m\alpha)} \frac{(-1)^{k+m'-m}}{k!(l+m-k)!(m'-m+k)!(l-m'-k)!} \sin\left(\frac{\beta}{2}\right)^{2k+m'-m} \cos\left(\frac{\beta}{2}\right)^{2l-2k-m'+m} =$$

$$= e^{i(m'\gamma+m\alpha)} d^l_{m',m}(\beta), \quad (2.8)$$

where $d^l_{m',m}$ are the elements of Wigner's (small) d-matrix, which are real expansions of sin and cos functions of the angle β. This matrix exhibits some symmetries, such as

$$d^l_{-m',-m}(\beta) = (-1)^{m-m'} d^l_{m',m}(\beta), \quad d^l_{m',m}(\beta) = (-1)^{m+m'} d^l_{m,m'}, \quad d^l_{m',m}(\beta) = d^l_{m,m'}(-\beta). \quad (2.9)$$

Explicit expressions for the matrix elements that are used in this project are

$$d^2_{2,2} = \cos^4\frac{\beta}{2}, \quad d^2_{1,2} = 2\cos^3\frac{\beta}{2}\sin\frac{\beta}{2},$$

$$d^3_{3,3} = \cos^6\frac{\beta}{2}, \quad d^3_{2,3} = \sqrt{6}\cos^5\frac{\beta}{5}\sin\frac{\beta}{2}, \quad (2.10)$$

$$d^4_{4,4} = \cos^8\frac{\beta}{2}, \quad d^4_{3,4} = 2\sqrt{2}\cos^7\frac{\beta}{5}\sin\frac{\beta}{2}, \quad d^4_{2,4} = 2\sqrt{7}\cos^6\frac{\beta}{2}\sin^2\frac{\beta}{2}.$$

Therefore, the rotation to obtain the modes in the quadrupole aligned frame can be written in terms of the Euler angles, resulting

$$\widehat{h}^{l,m} = \sum_{m'} h^{l,m'} \mathcal{D}^{(l)}_{m',m}(-\gamma, -\beta, -\alpha). \quad (2.11)$$

This last expression gives the quadrupole maximized modes, which are similar to those obtained for non-precessing systems and hence, present approximately the features that had been introduced [Eqs. (2.2) and (2.3)]. In addition, rotated modes can be determined analytically and compared easily, such as is the case for non-precessing waveforms.

3 Complex description of rotations

3.1 Quaternions

The rotation group $\mathbb{SO}(3)$ introduced in the previous section can be also parameterized by the set of unit quaternions. Quaternions were first described by William Rowan Hamilton in 1843 in order to obtain the analogues of complex numbers (points in the plane) but with points in a three dimensional space. They form a four-dimensional division algebra, which is associative but not commutative, over the real numbers. Quaternions can be expressed as $a + bi + cj + dk$, where a, b, c, d are real numbers and i, j, k are symbols that can be interpreted as unit vectors pointing along the spatial axes. In addition, $\{1, i, j, k\}$

form a basis of the 4-dimensional vector space over the real numbers. Another way to express quaternions is considering a scalar plus a vector

$$Q = q_0 + \vec{q} = \begin{bmatrix} q_0 \\ q_1 \\ q_2 \\ q_3 \\ q_4 \end{bmatrix}. \tag{3.1}$$

Their multiplication rule is what makes quaternions unusual, known as the *Hamilton product*

$$P \cdot Q = (p_0 q_0 - \vec{p} \cdot \vec{q}) + (p_0 \vec{q} + q_0 \vec{p} + \vec{p} \times \vec{q}). \tag{3.2}$$

Defining the conjugate of the quaternion as $\bar{Q} = q_0 - \vec{q}$, the norm is defined as the square root of the scalar product between a quaternion and its conjugate

$$\|Q\| = \sqrt{Q\bar{Q}} = \sqrt{q_0^2 + q_1^2 + q_2^2 + q_3^2}. \tag{3.3}$$

Unit quaternions are those whose norm (Eq. (3.3)) is equal to 1, which can be thought of as points on the unit 3-sphere. This set can be chosen as a group structure on the 3-sphere S^3. In a 4-dimensional space, the 3-sphere is the set of points equidistant from a fixed central point. More technically, it is a three-dimensional manifold (topological space which locally resembles flat space (Euclidean geometry)), which is compact and simply connected. The latter implies that any loop can be continuously shrunk to a point. This group is isomorphic to the 3D rotation group introduced in the previous section, $\mathbb{SO}(3)$, which gives rise to quaternion applications in different fields and the feature which we want to exploit in this project. An overview of applications of quaternions in physics is given in [42], including the discussion of its group representation applied to crystallography, the kinematics of the rigid body, and also the representation of the Lorentz group of special relativity. In addition they are related to spinors, which are fundamental objects in quantum theory.

In this section, it will be shown how a problem can be simplified through the use of complex variables. First, we will explore the Lorentz transformations, explaining some of the results demonstrated in [43], and finally, the benefits of using them for describing spatial rotations, deriving the expressions of the section above now using quaternions.

Before focusing on the description of spatial rotations in terms of quaternions, we illustrate the utility of complexifications through the example of Lorentz transformations. These describe the relation between observations made in two different inertial frames consistent with special relativity. Usually these transformations are presented in the simple case when the boost (relation between the movement of both frames) is aligned with one of the spatial coordinates. The simplicity disappears for the general Lorentz transformation, when six parameters are needed in order to describe the transformation: three for the relative velocity and three for describing the relative orientation of the frames. However, the use of complex variables can simplify the problem. A Lorentz transformation is a linear transformation of the real coordinates of an event to new coordinates (those measured in another frame), where both coordinates satisfy the relation

$$t'^2 - x'^2 - y'^2 - z'^2 = t^2 - x^2 - y^2 - z^2. \tag{3.4}$$

The most compact way to describe a Lorentz transformation is to arrange the original and transformed coordinates in columns and express the boost as a matrix (which contains

the details of the transformation), so the relation between both frames becomes

$$\mathbb{X}' = \mathbb{L}\mathbb{X}, \tag{3.5}$$

where $\mathbb{X}$ is a four row column and $\mathbb{L}$ is a 4×4 matrix. However, the general Lorentz transformation is rarely found written out explicitly due to its high complicity. The "complex" alternative consists in packing the coordinates into a 2×2 matrix

$$\mathbb{X} = \begin{bmatrix} t+z & x+iy \\ x-iy & t-z \end{bmatrix}. \tag{3.6}$$

In this new convention, a proper Lorentz transformation is defined as any linear transformation from t, x, y, z to t', x', y', z' which satisfies

$$\mathbb{X}' = \mathbb{A}\mathbb{X}\mathbb{A}^{\dagger}, \tag{3.7}$$

where $\mathbb{A}^{\dagger}$ is the Hermitian conjugate of the matrix $\mathbb{A}$, defined as

$$\mathbb{A} = \begin{bmatrix} a & b \\ c & d \end{bmatrix}, \tag{3.8}$$

where a, b, c, d are complex numbers. The condition (3.4) implies that (for a mathematical development see e.g. [43]):

$$ad - bc = 1. \tag{3.9}$$

Therefore, the 6 parameters needed are encoded in four complex numbers with two constrains given by Eq. (3.9) (for the real and complex part). This reduction of parameters has huge benefits for calculating the transformations in the most difficult cases, in which the usual convention (Eq. (3.5)) becomes complicated. Some examples can be found in [43], showing how simplification can be found through complexification. Furthermore, boosts in Lorentz transformations can be thought of as hyperbolic rotations of space-time coordinates in a four-dimensional Minkowski space. Since generators of 4D rotations can be represented by pairs of unit quaternions, any Lorentz transformation can then be related to quaternions [44].

3.2 Quaternions in spatial rotations

Turning to the description of spatial rotations, quaternions offer a number of advantages to describe spatial rotations over the use of Euler angles. First, their representation is more compact and they can be quicker to compute than the representation by matrices and in terms of trigonometric functions of Euler angles. Furthermore, they do not have the singularities of the Euler angle coordinates, which result in the phenomenon known as *gimbal lock*. It implies a loss of one degree of freedom in a system of three gimbals, which is the case when using Euler angles. The gimbal lock occurs when two of the three gimbals are in a parallel configuration, so the rotation can not be about one axis: the rotation takes place in a degenerate two-dimensional space. Some examples of these singularities will be seen in Section 4. Another convenience of using quaternions instead of Euler angles is their simplicity to compose rotations: while using Euler angles means multiplying matrices, composing rotations with quaternions is a vector multiplication. Therefore, this suggests that using quaternions in order to obtain the quadrupole aligned frame can be more efficient than using the usual representation explained in the section

above. It is for this reason that e.g. in computer graphics quaternions are already the standard way to rotate objects.

Any rotation in a three-dimensional space of a rigid body where a point remains fixed can be described by three Euler angles. These three composed rotations are equivalent to a single rotation about an axis that runs through the fixed point, according to Euler's rotation theorem. The fixed axis is called the Euler axis, denoted as $\hat{u}$ (which is a unit vector), and ϕ is the angle rotated about this axis. Quaternions provide a simple way to describe this rotation in terms of $\hat{u}$ and ϕ:

$$R = \cos\frac{\phi}{2} + \hat{u}\sin\frac{\phi}{2}. \tag{3.10}$$

This quaternion can be applied to a vector $\vec{v}$ (which can be considered as a quaternion with vanishing real part) to obtain the rotated vector $\vec{v}'$

$$\vec{v}' = R \cdot \vec{v} \cdot \bar{R}, \tag{3.11}$$

where $\cdot$ is the Hamilton product given in Eq. (3.2). Using this last expression, it is straightforward to show that the quaternion described in Eq. (3.10) effectively rotates the vector by ϕ around the $\hat{u}$ axis.

The composition of rotations using quaternions can be derived easily from expression (3.11). If the new vector $\vec{v}'$ is now rotated by θ about an axis $\hat{w}$, defining $P = \cos\frac{\theta}{2} + \hat{w}\sin\frac{\theta}{2}$, the rotated vector $\vec{v}''$ becomes

$$\vec{v}'' = P \cdot \vec{v}' \cdot \bar{P} = P \cdot R \cdot \vec{v} \cdot \bar{R} \cdot \bar{P} = (PR) \cdot \vec{v} \cdot \overline{PR}. \tag{3.12}$$

As a generalization of this last expression, the composition is the Hamilton product between the rotations following the corresponding order, taking into account that the product is not commutative.

In precessing binaries, Euler angles associated to the rotation of the inertial frame to the quadrupole aligned one can be obtained using the relations from Eq. (2.5) to Eq.(2.7). These angles (α, β, γ) represent rotations about the z, y and z-axis, respectively. In terms of quaternions, these rotations can be written as

$$\begin{aligned}
Q_1 &= \cos\frac{\alpha}{2} + \hat{z}\sin\frac{\alpha}{2}, \\
Q_2 &= \cos\frac{\beta}{2} + \hat{y}\sin\frac{\beta}{2}, \\
Q_3 &= \cos\frac{\gamma}{2} + \hat{z}\sin\frac{\gamma}{2},
\end{aligned} \tag{3.13}$$

where $\hat{z}$ and $\hat{y}$ are the unit vectors along the z and y axis. Therefore, the quaternions associated to these successive rotations are the composition of them, following Eq. (3.12):

$$R = Q_3 \cdot Q_2 \cdot Q_1 = \begin{bmatrix} \cos\frac{\alpha}{2}\cos\frac{\beta}{2}\cos\frac{\gamma}{2} - \cos\frac{\beta}{2}\sin\frac{\alpha}{2}\sin\frac{\gamma}{2} \\[2mm] \cos\frac{\gamma}{2}\sin\frac{\alpha}{2}\sin\frac{\beta}{2} - \cos\frac{\alpha}{2}\sin\frac{\beta}{2}\sin\frac{\gamma}{2} \\[2mm] \cos\frac{\alpha}{2}\cos\frac{\gamma}{2}\sin\frac{\beta}{2} + \sin\frac{\alpha}{2}\sin\frac{\beta}{2}\sin\frac{\gamma}{2} \\[2mm] \cos\frac{\beta}{2}\cos\frac{\gamma}{2}\sin\frac{\alpha}{2} + \cos\frac{\alpha}{2}\cos\frac{\beta}{2}\sin\frac{\gamma}{2} \end{bmatrix}. \tag{3.14}$$

This last expression gives the quaternion associated to a particular rotation in terms of the Euler angles. Therefore, given the angles which rotate the modes to the quadrupole aligned frame, one can calculate the associated quaternions and perform the same calculations in terms of them, since it is a more compact and efficient way to do it. The precession of the orbital plane can be thus described using quaternions, rotating the angular momentum vector with Eq. (3.11).

However, in order to obtain the quadrupole modes given by the expression (2.4), Wigner matrices need to be expressed also in terms of quaternions. The easiest way to deduce the equivalent of Eq. (2.8) in terms of quaternions is inverting the relation found in Eq. (3.14), and substituting the results directly in (2.8). Using some trigonometric identities, it is straightforward to show that the Wigner matrix becomes

$$\mathcal{D}^{(l)}_{m',m}(q_0, q_1, q_2, q_3) = \sum_{k=\max[0,m-m']}^{\min[l+m,l-m']} \sqrt{(l+m)!(l-m)!(l+m')!(l-m')!}$$

$$\times e^{i((m'+m)\arctan\frac{q_3}{q_0}+(m-m')\arctan\frac{q_1}{q_2})}$$

$$\frac{(-1)^{k+m'-m}}{k!(l+m-k)!(m'-m+k)!)}\sqrt{1-(q_0^2+q_3^2)}^{-2k+m'-m}\sqrt{q_0^2+q_3^2}^{2l-2k-m'+m}$$

$$= e^{i((m'+m)\arctan\frac{q_3}{q_0}+(m-m')\arctan\frac{q_1}{q_2})}d^l_{m',m}(q_0, q_3), \quad (3.15)$$

where again $d^l_{m',m}$ are the elements of the Wigner's (small) d-matrix, but in terms of quaternions. Some explicit expressions for these matrix elements are

$$d^2_{2,2} = (q_0^2+q_3^2)^2, \quad d^2_{1,2} = 2(q_0^2+q_3^2)^{3/2}\sqrt{1-q_0^2-q_3^2},$$

$$d^3_{3,3} = (q_0^2+q_3^2)^3, \quad d^3_{2,3} = \sqrt{6}(q_0^2+q_3^2)^{5/2}\sqrt{1-q_0^2-q_3^2},$$

$$d^4_{4,4} = (q_0^2+q_3^2)^4, \quad d^4_{3,4} = 2\sqrt{2}(q_0^2+q_3^2)^{7/2}\sqrt{1-q_0^2-q_3^2}, \quad d^4_{2,4} = 2\sqrt{7}(q_0^2+q_3^2)^3(1-q_0^2-q_3^2).$$

$$(3.16)$$

These matrices can be computed more efficiently and accurately using quaternions than the Euler angles as can be seen by comparing expressions from (2.10) and (3.16). While using Euler angles these matrix elements are expansions of trigonometric functions, in terms of quaternions they are simply polynomial functions. Finally, the rotated modes can be obtained in this case (see Eq. (2.4)) as

$$\widehat{h}^{l,m} = \sum_{m'} h^{l,m'}\mathcal{D}^{(l)}_{m',m}(q_0, -q_1, -q_2, -q_3). \quad (3.17)$$

4   Twisting up Gravitational Waves

We now turn to the application of quaternions to describe rotations in the context of precession. These transformations have been implemented as Mathematica code, both in terms of Euler angles and quaternions. Given a waveform from a precessing system and the Euler angles which decompose it to the quadrupole aligned frame, the respective quaternions have been calculated using Eq. (3.14). The quadrupole modes have been computed following Eqs. (2.11) and (3.17) based on implementations of the Wigner Matrices in terms of Euler angles (2.8) and quaternions (3.15). Results have been tested by comparing them to each other and also to previous Euler angle implementations of the

group. Additionally it has been checked that the twisting up of non-precessing waveforms commutes with the quadrupole alignment transformation into a co-rotating frame. We will first consider two example waveforms obtained from numerical relativity simulations, where we will check how the transformation to the quadrupole-aligned frame will simplify the mode structure, and compare the Euler angle and quaternion descriptions. We will then compare the two descriptions for post-Newtonian waveforms, where long waveforms corresponding to challenging situations can be computed within minutes.

4.1 Numerical relativity waveforms

This section applies the quadrupole aligned frame method (using Euler angles and quaternions) to two numerical relativity waveforms produced by the SpEC code [45], which uses pseudo-spectral methods to solve the Einstein equations. These waveforms are publicly available [46]. Two precessing waveforms are considered here. For the first one (SXS:BBH:0037), only the heavier of the two BHs is spinning, while for the second one (SXS:BBH:0053) both BHs are spinning. All the spins are initially located within the orbital plane and both binary systems have a mass ratio of $q = 3$. In order to show the efficiency of the method, rotated waveforms are compared with the waveform coming from a non-spinning source of equal mass ratio (SXS:BBH:0030), which is the non-precessing waveform that corresponds to the two precessing waveforms in the quadrupole-aligned frame.

In numerical relativity, it is useful to use the Newman-Penrose formalism [47], which introduces spinors in order to treat general relativity. Weyl scalars refer to a set of 5 complex scalars $\{\Psi_i\}$ which encode the ten independent components of the Weyl tensor (equivalent of the Riemann curvature tensor). The Weyl Scalar Ψ_4 encodes the outgoing gravitational radiation of an asymptotically flat system. In fact, this scalar is given by

$$\Psi_4 = -\ddot{h} = -\ddot{h}_+ + i\ddot{h}_\times. \tag{4.1}$$

If h is the strain of the wave, which measures the difference between both arms in the interferometer, then the Weyl scalar is a measure of the its acceleration. In numerical relativity, the Weyl scalar is easier to compute, and in order to obtain the strain it is necessary to integrate twice the data obtained. Thus, in this section we will plot this scalar instead of the strain of the wave. However, the decomposition in terms of the spherical harmonics is the same as in Eq. (2.1), so the rotated modes can be found in the same way as in Eq. (2.4), substituting $h \to \Psi_4$ and $h^{l,m} \to \Psi_{4,lm}$.

For numerical relativity waveforms, the inertial frame is usually defined by the initial orbital angular momentum, which has been denoted as the L_0 frame. In this frame, the spin components are approximately preserved. Hence, if the spins only have components perpendicular to the orbital angular momentum, the waveform in the co-precessing frame is the same as the one produced by a non-spinning source (note the difference between non-precessing, which may have spins orthogonal to the orbital plane, and non-spinning, which does not have spins). In this frame, the second Euler angle is denoted as ι and parametrizes the opening between the orbital angular momentum at each instant of time with the initial one. Although this frame is the simplest choice to describe the spin components, this does not occur for the waveform. If L_0 is the inertial frame in which the waveform is initially decomposed, then the Euler angle ι becomes sharp and the procedure fails when it becomes higher than $\pi/2$. However, if a smart choice of fixed axes is made, then the waveform becomes simpler and so do the second Euler angle. Comparisons between choosing the inertial frame J_0 or L_0 are done in Sec. 4.2.

4.1.1 Single spin case (SXS:BBH:0037)

This numerical relativity waveform is from a black hole binary, where the largest one has initial dimensionless spin $\chi_1 = \frac{\mathbf{S_1}}{Gm_1^2} = 0.5\hat{x}$, i.e. orthogonal to the orbital angular momentum. Therefore, this system presents the spin precession phenomenon according to Equation (1.22).
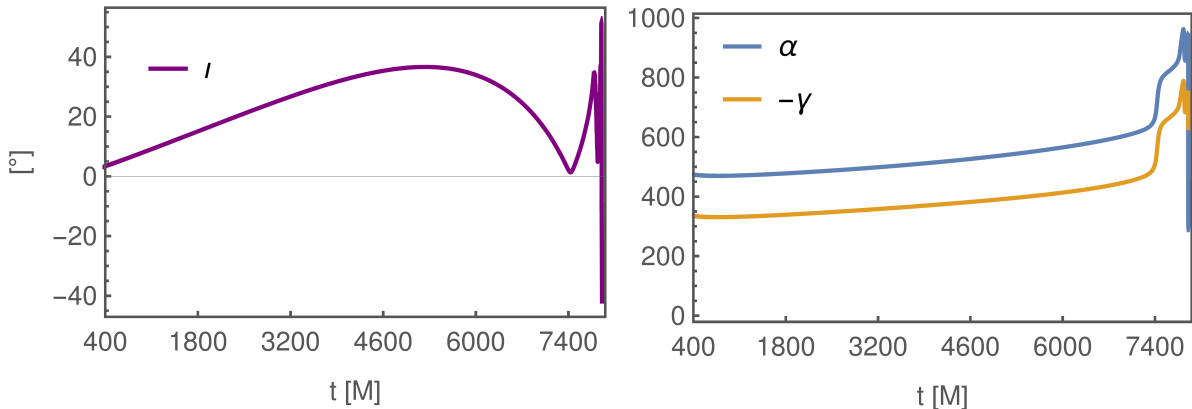

Figure 5: Evolution of the Euler angles which rotate the waveform to the quadrupole aligned frame in terms of the time, measured in units of mass. These angles have been obtained from the $(2,2)$-maximization procedure for the single spin waveform SXS:BBH:0037. The time starts at 400 [M] in order to avoid noise fluctuations at low frequencies, and finishes 180 [M] after the peak of the strain associated to the merger (7776.98 [M]). This is the convention used in all plots to easily compare waveforms.

Figure 5 shows the evolution of the Euler angles that transform the SXS:BBH:0037 waveform to the quadrupole aligned frame. The time starts at 400 [M] to avoid initial transient noise. Due to the high sensitivity required of the detectors, they can detect any external noise which becomes present at the lowest levels of the detected gravitational wave, called artificial gravitational waves. This noise has larger effects on the lower modes and decays as the amplitude of the wave increases, as shown in Figs. 7 and 11. On the other hand, during the ringdown of the resulting compact object, there are excited constant frequency modes which are however not the spherical harmonics in which the waveform has been decomposed. Moreover, these modes do not form a basis since they are not orthogonal. For this reason, mode mixing occurs in the spherical harmonic modes, which produces modulations of the waveform during this last stage, which have also been removed. The left panel exhibits the angle ι, and as expected, it begins at 0°. It evolves smoothly until there is a sudden change at a time of approximately 7400 [M]. The fact that the second Euler angle is not typically negative during the inspiral creates this sharp reflections. The right panel shows the α and $-\gamma$ angles, which have a smooth evolution until the moment of the fusion approaches. Both have been offset by $\pm 360°$, respectively, so that they do not change sign. The great resemblance between $-\gamma$ and α is because the evolution of γ was obtained from Eq. (2.6). The gimbal lock problem occurs when the second Euler angle exceeds $\pi/2$, and above this value the quadrupole aligned method fails. This case of mass ratio 3 already presents a challenging evolution, which suggests that more extreme cases may lead to values of ι larger than $\pi/2$.

Given the Euler angles plotted in Figure 5, the associated quaternions can be computed using Eq. (3.14), giving the result shown in Figure 6.
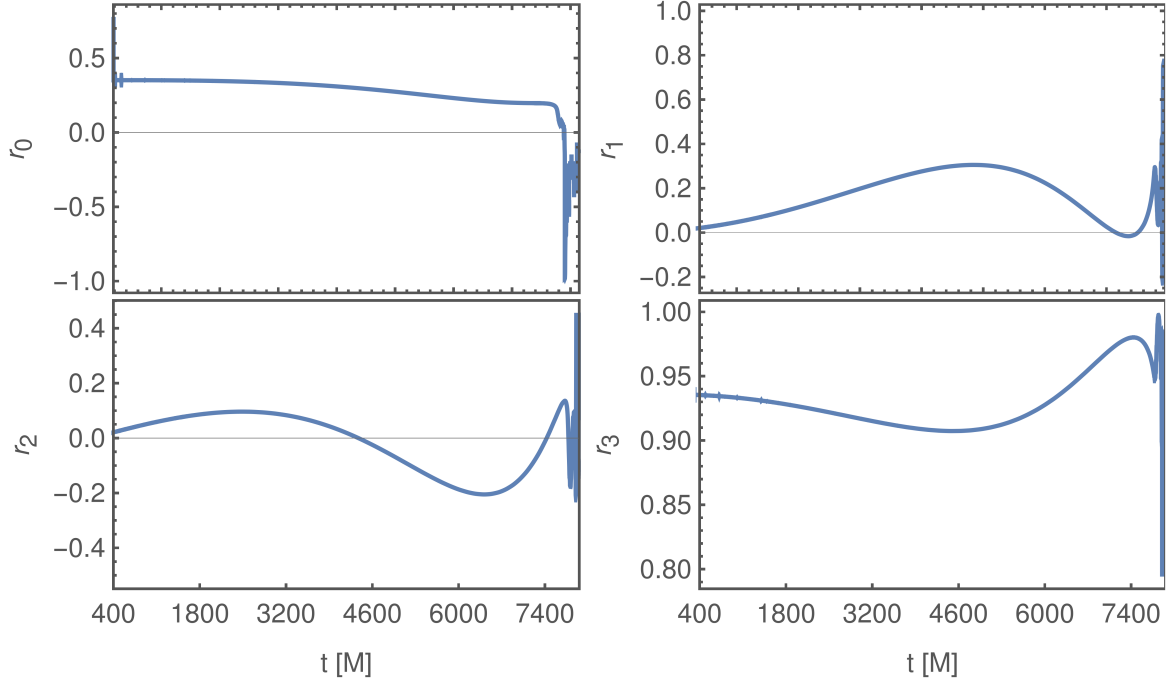
Figure 6: Evolution of the quaternion components which rotate the waveform to the quadrupole frame in time, measured in units of mass. The quaternion components have been computed using Eq. (3.14) with the Euler angles shown in Figure 5.
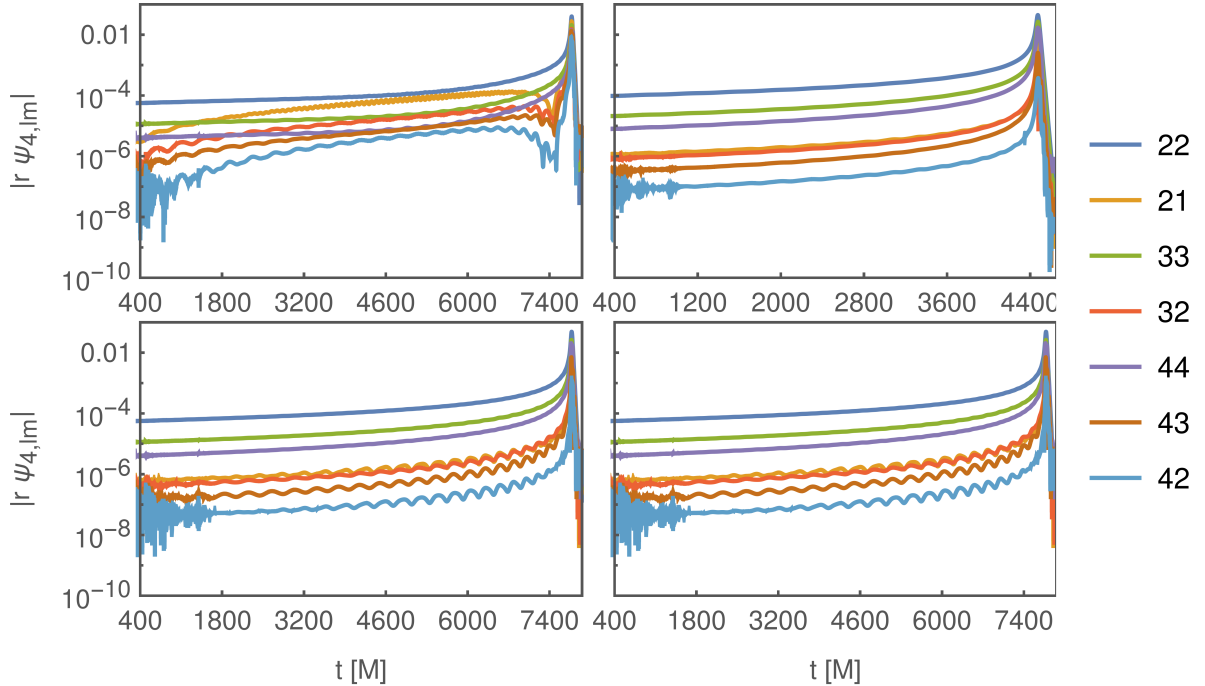

Figure 7: Time evolution of the amplitudes for the dominant mode $\Psi_{4,22}$ and selected subdominant modes in logarithmic scale. *Top row*: Comparison between the amplitudes from the SXS:BBH:0037 waveform (*left*) and SXS:BBH:0030 (*right*). *Bottom row*: Comparison between the rotated amplitudes from the SXS:BBH:0037 data into the quadrupole aligned frame, computing Eq. (2.11) with Euler angles in Fig. 5 (*left*), and computing Eq. (3.17) with quaternions in Fig. 6 (*right*).

In contrast to the Euler angles, quaternions do not suffer from coordinate problems when performing rotations. Thus, they present a more robust way to execute the quadrupole aligned method. Even though this is only an example, quaternions present the same features in any situation, both for highly precessing waveforms and for any fixed frame. Following examples will reinforce quaternion compactness and effectiveness.

Nevertheless, for this specific waveform both implementations achieve an accurate quadrupole aligned waveform which is equivalent to that coming from a non-spinning system, as shown in Figure 7. This agreement between both waveforms is due to the choice of the fixed frame L_0. The top left panel shows the evolution of the dominant mode $(2, 2)$ and other subdominant modes for the waveform in this inertial frame. Even though the dominant amplitude and the highest modes present features compatible with those coming from non-precessing systems, lower modes show modulations which complicate the understanding of the waveform. The top right panel shows the numerical relativity waveform SXS:BBH:0030, which exhibits a smooth increase until the peak associated to the merger of the black holes, followed by the exponential decrease of the waveform (since it is plotted in logarithmic scale). Quadrupole aligned waveforms obtained using Euler angles (bottom left panel) or quaternions (bottom right panel) exhibit the same features as the non-spinning one, where the modulations on lower modes present on the original waveform have been removed. We can thus conclude that the method proposed is effective since it achieves the expected results, both the concordance between rotations with EA or quaternions and also with the SXS:BBH:0030 data.

Finally, the quadrupole aligned frame decomposes the modes in a similar way to those coming from a non-precessing system, which implies that they approximately satisfy the symmetry property given by Eq. (2.2). Figure 8 shows the difference between the amplitudes of the $|m|$ modes for selected modes which did not present high modulations during a period close to the merger. Left column of panels shows how this property does not hold for precessing waveforms, while quadrupole aligned modes show a higher degree of symmetry between $\pm m$ modes (right panels). The fact that precessing waveforms do not present symmetry respect to the $|m|$ modes implies that stronger radiation can be either toward the north or south. When both black holes are orbiting to each other, during the middle part of the orbit emit the positive modes and then the negative ones. If there is an asymmetry between the quantity of gravitational radiation emitted, then both contributions do not cancel so the remnant black hole of the fusion will have a recoil velocity perpendicular to the orbital plane in the direction of maximum emission. Thus, the amount of linear momentum in the z' direction of the final object can be computed easily from the difference between the energy of the $(l, \pm m)$ modes, considering the relativistic relation between energy and momentum. An example of the simplest case where only the dominant $(2, |2|)$ modes are considered can be found in Section III A in [48]. Rotated modes, shown in the right panels of Figure 8, present approximately the feature expected for non-precessing systems, but any rotation can not completely eliminate the asymmetries of precessing waveforms. However, the fact that the method produces higher modes consistent with those from non-precessing waveforms permits the complete representation of the waveform in a simpler way than the one produced directly by the numerical relativity code. The possibility to compute the subdominant modes of precessing binaries twisting up a non-precessing waveform simplify the production of analytical binary coalescence methods.
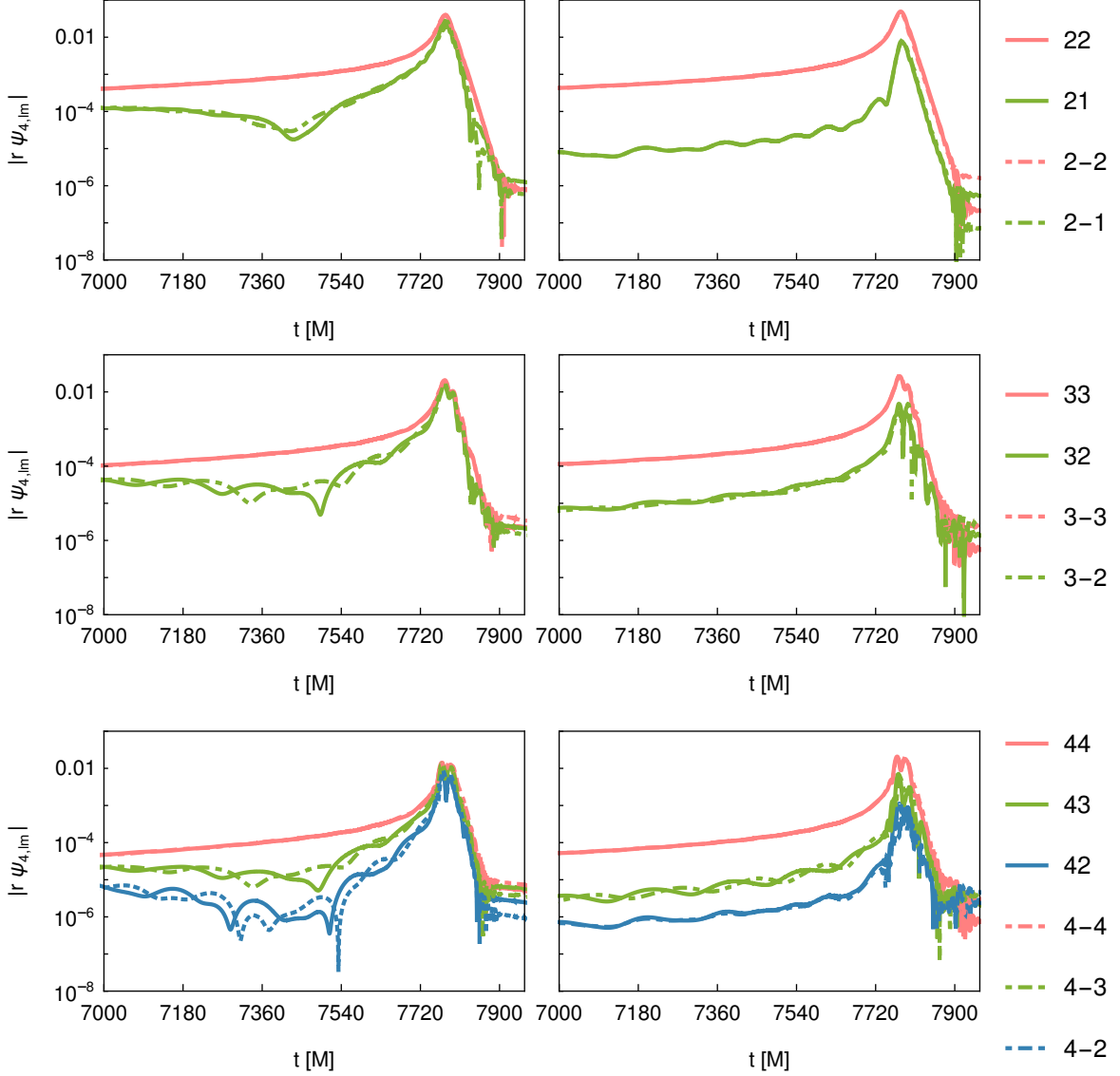
Figure 8: Difference between the amplitudes (in logarithmic scale) of the (l, m) and $(l, -m)$ modes for the SXS:BBH:0037 data close to the merger. Only those modes which does not present noise fluctuations have been plotted for each l. *Left column*: selected modes of the precessing waveform. *Right column*: selected modes of the same waveform after being transformed into the quadrupole aligned frame. These rotated waveforms approximately present the expected feature for non-precessing binaries (Eq. (2.2)).

These results show the robustness of the quadrupole aligned method, both for Euler angles and quaternions. Moreover, a mass ratio of 3, which is not an extreme case, produce modulations in the second Euler angle. This suggests that larger mass ratios may conduce to the gimbal lock problem, since highly precessing waveforms difficult the ι evolution. Therefore, extreme cases could not permit using Euler angles in the procedure, while quaternions work in any situation. Some of these challenging examples have been developed as post-Newtonian waveforms, which not only show how the Euler angles become wilder but also how an appropriate inertial frame can simplify them.

Next numerical relativity waveform performs another test of the method which shows the possibility to obtain a "normal form" for all waveforms with the same mass ratio, precessing or not, which facilitate comparisons between analytical and numerical results.

4.1.2 Double spin case (SXS:BBH:0053)

SXS:BBH:0053 numerical waveform corresponds to a black hole binary where both BHs have initial dimensionless spins within the orbital plane. In particular, the larger BH has $\chi_1 = 0.5\hat{x}$, while the smaller, $\chi_2 = -0.5\hat{x}$. Again, according to Eq. (1.22), the system shows spin precession, so the same analysis can be done in this double spin case. Moreover, since the spins only have perpendicular components to the orbital angular momentum, then the quadrupole aligned waveform corresponds to the same non-spinning waveform SXS:BBH:0030.
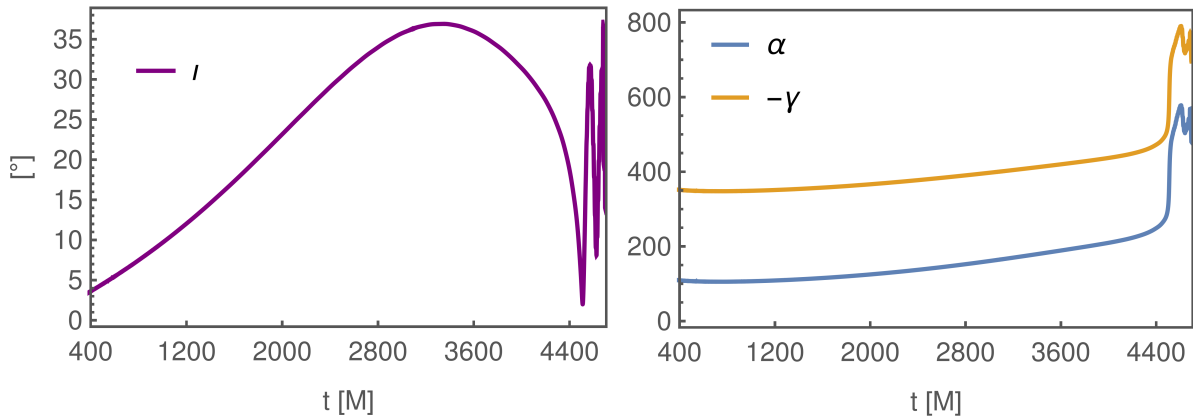

Figure 9: Evolution of the Euler angles which rotate the waveform to the quadrupole frame in time, measured in units of mass. These angles have been found from the (2,2)-maximization procedure for the double spin waveform SXS:BBH:0053. The peak of the strain in this case corresponds to t=4526.96 [M].
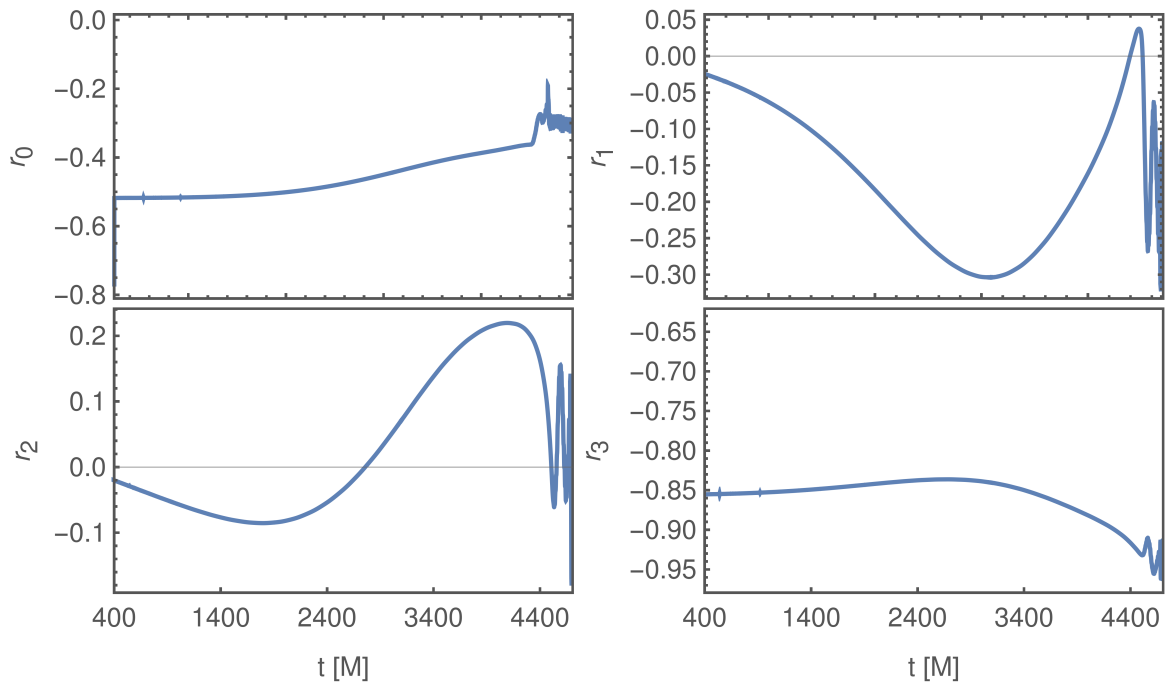

Figure 10: Evolution of the quaternion components which rotate the waveform to the quadrupole frame in terms of the time, measured in units of mass. The quaternions have been computed using Eq. (3.14) with the Euler angles shown in Figure 9.
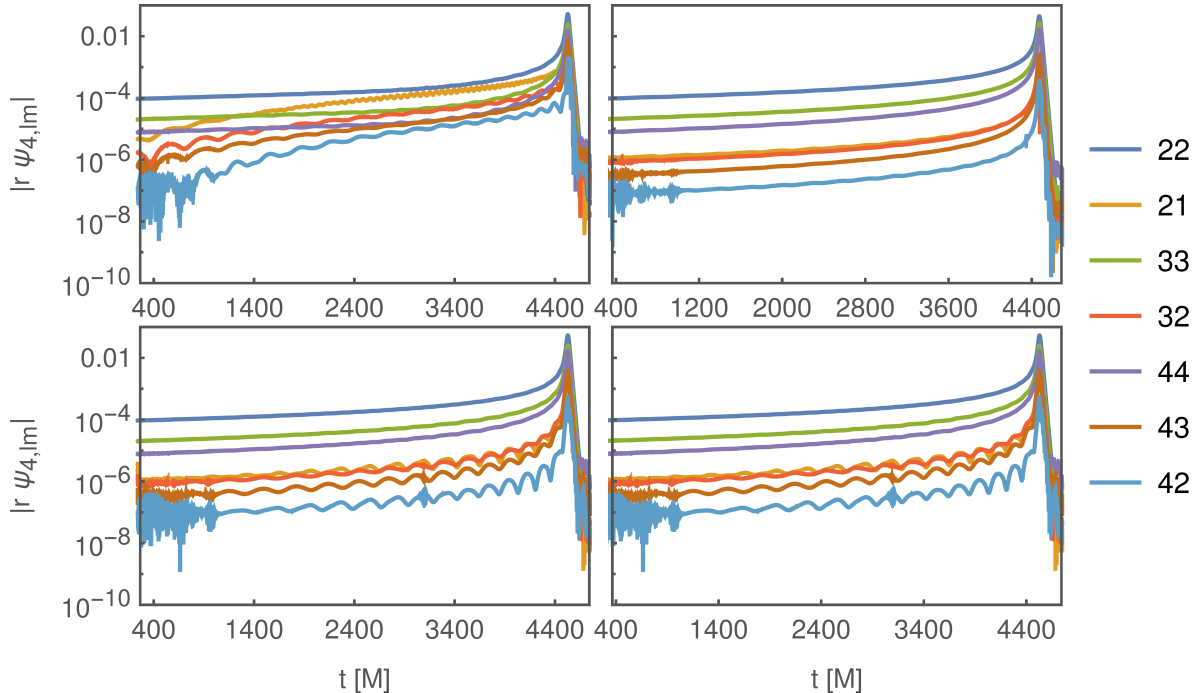
29

Figure 11: Time evolution of the amplitudes for the dominant mode $\Psi_{4,22}$ and selected sub-dominant modes. *Top row*: Comparison between the amplitudes from the SXS:BBH:0053 waveform (*left*) and SXS:BBH:0030 (*right*). *Bottom row*: Comparison between the rotated amplitudes from the SXS:BBH:0053 data, computing Eq. (2.11) with Euler angles in Fig. 9 (*left*), and computing Eq. (3.17) with quaternions in Fig. 10 (*right*).

The results found for this new case have the same features than the latter. This agreement is because the fact that only one or both BHs have spin do not have a big impact on the evolution equations. The spins of both black holes together with the mass ratio q give the effective spin (Eq. (1.21)), which determines either the evolution of the coalescence (Eq. (1.20)) and also the precession of the orbital plane (Eq. (1.22)). Therefore, the only difference between this case and the one developed above is that the second term in Eq. (1.21) contributes. However, this effect does not have great impact, so the evolution of the Euler angles (Figure 5) and quaternion components (Figure 10) show the same behaviour. Finally, Figure 11 exhibits remarkable agreement between rotated modes (bottom row) and the modes of the non-spinning waveform (top right panel), and hence, with the rotated modes in Fig. 8. This fact shows the benefit of the quadrupole aligned method: any precessing waveform can be decomposed to the one produced by the same system but non-precessing, independently of the perpendicular spin components of the black holes involved.

4.2 Post-Newtonian waveforms

The examples above have demonstrated the effectiveness of the proposed method and how quaternions work as well as Euler angles. However, quaternions have not played a different role than the Euler angles. SXS waveforms suggest that in extreme cases, where q becomes high enough and thus the waveform becomes highly precessing, the second Euler angle may cause problems during the twisting up procedure. This section explores the evolution of a post-Newtonian waveform coming from a precessing system with mass ratio $q = 7.5$ and how by considering an appropriate inertial frame, the waveform is simplified.
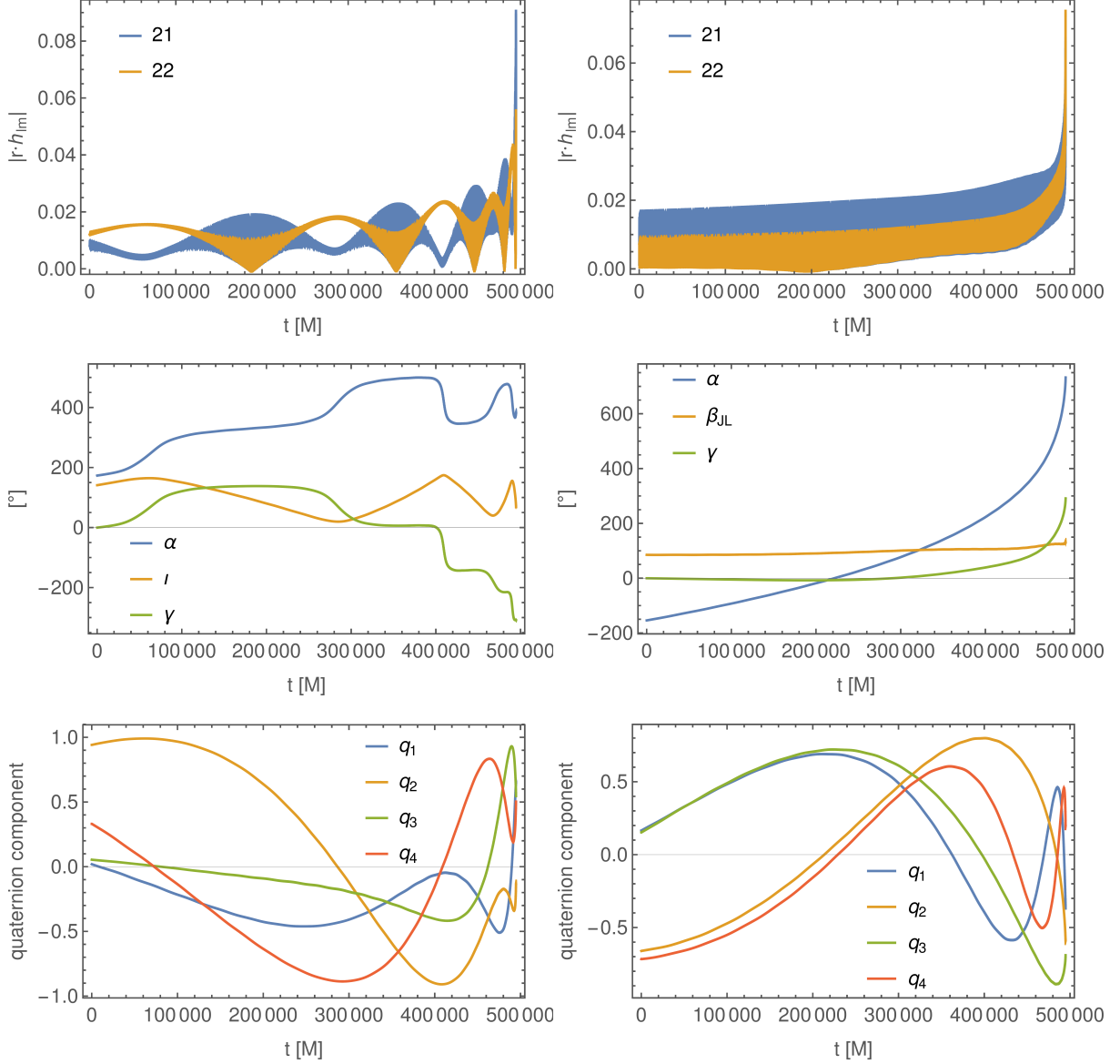
Figure 12: Comparison between the features of the waveform from a precessing-binary system of $q = 7.5$ in the L_0 frame (*left column*) and the J_0 frame (*right column*). *First row*: Evolution of the post-Newtonian waveform in both frames. *Second row*: Evolution of the Euler angles which rotate the previous waveforms to the quadrupole aligned frame. *Third row*: Evolution of the quaternions, obtained from the Euler angles above.

Figure 12 shows how the same system analyzed from two different inertial frames present distinctive features. Usual SXS definition of the inertial frame (left panels), the L_0 frame characterized by the z-axis aligned with the initial angular momentum, produces an intricate waveform and hence, a complex evolution of the Euler angles. However, defining the z-axis as the direction of the total angular momentum, the J_0 frame, simplifies the waveform and also the evolution of the Euler angles (in this case, the second one is referred to as β_{JL}). Regarding to quaternions, they exhibit the same sort of evolution in both frames, implying that their effectiveness does not depend on this election. In fact, even in the L_0 frame, where the waveform and the Euler angles become "wilder", quaternions are not affected and present the smooth evolution shown for the J_0 frame. Thus, quaternions prove to be a more general way of finding the co-precessing frame, whereas the Euler angles can fail if a smart choice of coordinates has not been made.

5 Discussion

This work applies the quadrupole aligned method to track the precession of the orbital plane, which consists in decomposing the waveform into a non-inertial time-dependent frame where it becomes more manageable. The procedure rotates the system maximizing the amplitude of the dominant modes $(2, \pm 2)$, so the rotated waveform is similar to the one produced by the same system without precession, i.e. with both black hole spins parallel to the orbital angular momentum. Both the dominant and subdominant modes thus become consistent with what is already known from non-precessing systems. This fact permits to represent the waveform more simply and facilitates comparisons between analytical and numerical results.

The main difference between previous applications of the method and the one proposed in this project is the use of quaternions to do the rotations, instead of the Euler angles. Quaternions present a more compact and efficient way to rotate the system since they do not have a preferred frame. Moreover, unlike with the Euler angles, rotations with quaternions avoid coordinate problems, so even in the most extreme cases quaternions work accurately to obtain the quadrupole aligned waveform. The intricate evolution of the Euler angles that leads to problems when performing the twisting-up procedure depends however on the inertial frame chosen.

Work in this project has proceeded in three steps. First, Mathematica code was developed to implement quaternion algebra and to perform waveform frame rotations with quaternions, and the code was extensively tested. In the second step the code was applied to numerical relativity waveforms, and in a third step to much longer waveforms obtained from the post-Newtonian approximation. When treating numerical relativity waveforms from SXS simulations, the inertial frame is defined by aligning the z-axis with the initial orbital angular momentum, which makes the Euler angles become "wilder". When the second Euler angle ι becomes larger than $\pi/2$, the method fails due to the gimbal lock problem. In these cases, the use of quaternions becomes essential because they work for generically precessing waveforms. In fact, only the quaternion description can perform SXS numerical relativistic simulations of highly-precessing waveforms.

Nevertheless, the Euler angle problems can be solved by choosing an appropriate inertial frame, as shown in Figure 12. Post-Newtonian waveforms are usually described in the inertial frame defined by the total angular momentum, called J_0. In this frame, the waveform is more manageable than in the L_0 frame, and thus, the second Euler angle evolution is smoother, what complicates acquiring the problematic value of $\pi/2$. Therefore, quaternions are not indispensable when treating PN waveforms since obtaining a challenging evolution of the second Euler angle β_{JL} is not only infrequent but also laborious to develop. Thus, the fact that SXS numerical relativity waveforms need the quaternion description to solve the most extremely precessing systems suggests that it would be better to first rotate the waveform into the J_0 frame. Since all current codes are implemented in terms of the Euler angles, using the quaternion description implies obtaining their components in the first place. Thus, to deal with gravitational waves currently detectable by our instruments it is easier to consider the waveform in the inertial J_0 frame, which usually does not present problems with the Euler angles. However, the implementation of the quaternion representation in analytical models would present enhancements both in the possibility of solving any precessing waveform and in the efficiency of numerical expansions, as seen in Equation (3.16). Besides, quaternions are used primarily because of their effectiveness in computing rotations versus other techniques (e.g. in computer

graphics). Hence, the quaternion implementation could improve further the twisting up procedure.

Since current problems with Euler angles can be solved by smartly choosing the z-axis, switching to quaternions does not become an emergency, but a future proposal to deal with any type of system. Ground-based detectors have a limited range of detectable gravitational waves, but the upcoming incorporation of LISA will broaden this horizon. Hence, the available parameter space of the detections will increase, and so will the possibility of the Euler angle failure. To avoid being aware of whether the method works correctly, the full implementation of the quaternion description would be advantageous, both for analytical expansions of post-Newtonian and numerical relativity waveforms, and also to find the co-processing frame.

In conclusion, this project has illustrated the utility of the quadrupole aligned method, both using Euler angles and quaternions. Moreover, it has shown the generality of the quaternions comparing their description in two different frames. Unlike for the Euler angles, their effectiveness do not depend on the chosen inertial frame and they work for generically precessing waveforms. Current detectable gravitational waves allow the use of Euler angles because their associated problems can be solved by establishing an appropriate inertial frame, such as that defined by the total angular momentum. However, the approaching incorporation of the space-based detector will expand the detectable parameter space and thus, a quaternion description would be advisable to ensure an accurate twisting up performance for any system.

References

[1] The LIGO Scientific Collaboration and the Virgo Collaboration, Phys. Rev. Lett. **116**, 061102 (2016).

[2] B. P. Abbott et al., Phys. Rev. X **9**, 031040 (2019).

[3] A. Einstein, German, Sitzungsber. Preuss. Akad. Wiss. Berlin, 688–696 (1916).

[4] M. Sieniawska and M. Bejger, Universe **5**, 217 (2019).

[5] N. Christensen, Reports on Progress in Physics **82**, 016903 (2018).

[6] *LIGO Laboratory Caltech*, http://www.ligo.caltech.edu/news/ligo20200326.

[7] The LIGO Scientific Collaboration and The Virgo Collaboration, Phys. Rev. Lett. **119**, 161101 (2017).

[8] *KAGRA Large-scale Cryogenic Graviational wave Telescope Project*, https://gwcenter.icrr.u-tokyo.ac.jp/en/.

[9] *LISA Consortium*, https://www.lisamission.org/.

[10] A. Einstein, Sitzungsber. Preuss. Akad. Wiss. Berlin, 844–847 (1915).

[11] K. Schwarzschild, Sitzungsber. Preuss. Akad. Wiss. Berlin, 189–196 (1916).

[12] W. Israel, Phys. Rev. **164**, 1776–1779 (1967).

[13] B. Carter, Phys. Rev. Lett. **26**, 331–333 (1971).

[14] R. P. Kerr, Phys. Rev. Lett. **11**, 237–238 (1963).

[15] P. C. Peters, Phys. Rev. **136**, B1224–B1232 (1964).

[16] M. Maggiore, *Gravitational Waves (Volume I)* (Oxford University Press, 2007).

[17] L. Blanchet, Living Rev. Rel. **9**, 4 (2006).

[18] F. Pretorius, Phys. Rev. L **95**, 121101 (2005).

[19] M. Campanelli et al., Phys. Rev. L **96**, 111101 (2006).

[20] J. G. Baker et al., Phys. Rev. L **96**, 111102 (2006).

[21] A. Buonanno, Y. Chen, and T. Damour, Phys. Rev. D **74**, 104005 (2006).

[22] M. Hannam et al., Phys. Rev. L **113**, 151101 (2014).

[23] A. Bohé et al., PhenomPv2 - Technical notes for the LAL implementation (2016).

[24] L. London et al., Phys. Rev. Lett. **120**, 161102 (2018).

[25] G. Pratten et al., arXiv:2004.06503 (2020).

[26] D. V. Martynov et al., Phys. Rev. D **93**, 112004 (2018).

[27] L. Wainstein and V. Zubakov, *Extraction of Signals from Noise* (Prentice-Hall, Englewood Cliffs, NJ, 1962).

[28] É. É. Flanagan and S. A. Hughes, Physical Review D **57**, 4535–4565 (1998).

[29] B. Allen, Phys. Rev. D **71**, 062001, 062001 (2005).

[30] S. A. Usman et al., Class. Quant. Grav. **33**, 215004 (2016).

[31] J. Veitch et al., Phys. Rev. D **91**, 042003 (2015).

[32] P. Schmidt et al., Phys. Rev. D **84**, 024046 (2011).

[33] L. E. Kidder, Physical Review D **52**, 821–847 (1995).

[34] K. S. Thorne and J. B. Hartle, Phys. Rev. D **31**, 1815–1837 (1985).

[35] J. N. Goldberg, A. J. Macfarlane, E. T. Newman, F. Rohrlich, and E. C. G. Sudarshan, J. Math. Phys. **8**, 2155–2161 (1967).

[36] M. Favata, Class. Quantum Gravity **27**, 84036 (2010).

[37] M. Boyle et al., arXix:1409.4431 (2014).

[38] H. Estellés et al., arXiv:2004.08302 (2020).

[39] LIGO Scientific Collaboration, *LIGO Algorithm Library - LALSuite*, free software (GPL), 2018.

[40] M. Boyle, R. Owen, and H. P. Pfeiffer, Phys. Rev. D **84**, 124011 (2011).

[41] E. P. Wigner, *Group theory and its application to the quantum mechanics of atomic spectra* (Academic Press, New York, 1959), p. 372.

[42] P. R. Girard, EJPh **5**, 25–32 (1984).

[43] E. T. Newman and R. H. Price, Am. J. Phys. **78**, 14–19 (2010).

[44] P. A. M. Dirac, Proceedings of the Royal Irish Academy **50**, 261–270 (1944).

[45] B. Szilagyi, L. Lindblom, and M. A. Scheel, Phys.Rev. **D80**, 124010 (2009).

[46] M. Boyle et al., Class. Quant. Grav. **36**, 195006 (2019).

[47] E. Newman and R. Penrose, J. Math. Phys. **3**, 566–578 (1962).

[48] B. Brügmann et al., Physical Review D **77**, 124047 (2008).